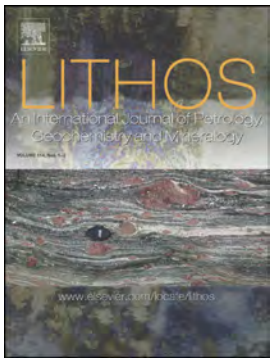

Trace element composition of amphibole and petrogenesis of hornblendites and plutonic suites of Cretaceous magmatic arcs developed in the Fuegian Andes, southernmost South America

M.F. Torres García, M. Calderón, C. Ramírez de Arellano, F. Hervé, J. Opitz, T. Theye, C.M. Fanning, R.J. Pankhurst, M. González-Guillot, F. Fuentes, M. Babinski

PII: S0024-4937(20)30293-0

DOI: https://doi.org/10.1016/j.lithos.2020.105656

Reference: LITHOS 105656

To appear in: *LITHOS*

Received date: 25 November 2019

Revised date: 28 March 2020

Accepted date: 20 June 2020

Please cite this article as: M.F.T. García, M. Calderón, C.R. de Arellano, et al., Trace element composition of amphibole and petrogenesis of hornblendites and plutonic suites of Cretaceous magmatic arcs developed in the Fuegian Andes, southernmost South America, *LITHOS* (2020), https://doi.org/10.1016/j.lithos.2020.105656

Trace element composition of amphibole and petrogenesis of hornblendites and plutonic suites of Cretaceous magmatic arcs developed in the Fuegian Andes, southernmost South America.

M.F. Torres García[a,*], M. Calderón[a], C. Ramírez de Arellano[a], F. Hervé[a,b], J. Opitz[c], T. Theye[c], C.M. Fanning,[d], R.J Pankhurst[e], M. González-Guillot[f,g], F. Fuentes[h], M. Babinski[i]

[a] Carrera de Geología, Universidad Andres Bello, Sazie 2119, Santiago, Chile

[b] Departamento de Geología, Universidad de Chile, Plaza Ercilla 803, Santiago, Chile

[c] Institut für Anorganische Chemie, Universität Stuttgart, Pfaffenwaldring 55, D-70569 Stuttgart, Germany

[d] Research School of Earth Sciences, The Australian National University, Canberra, ACT 0200, Australia

[e] Visiting Research Associate, British Geological Survey, Keyworth, Nottingham NG12 5GG, United Kingdom

[f] Centro Austral de Investigaciones Científicas (CADIC), CONICET, B. Houssay 200 (V9410BFD), Ushuaia, Argentina

[g] Instituto de Ciencias Polares, Ambiente y Recursos Naturales, Universidad Nacional de Tierra del Fuego, Fuegia Basquet 251 (V9410BFD), Ushuaia, Argentina

[h] Carrera Geología, Facultad de Ingeniería, Universidad Central, Chile

[i] Instituto de Geociências, Universidade de São Paulo, Rua do Lago 562, Cidade Universitária, CEP 05508-080, São Paulo, Brasil.

Abstract:

The evolution of continental crust in convergent margins can be explored in southernmost South America (54-56ºS). Plutonic rocks of the Fuegian Batholith and the rear-arc satellite Ushuaia Pluton were emplaced within the magmatic arc and the Fuegian fold-and-thrust belt, respectively. They record subduction zone processes in two distinct tectonic settings during the evolution of the Rocas Verdes Basin. We report new U-Pb zircon geochronology, bulk rock chemistry, Sr-Nd isotope data, and EPMA and in-situ LA-ICP-MS analyses of amphibole from ‗hornblendites' and gabbroic-granitoid suites in order to evaluate the origin and evolution of the magmatic plumbing systems in the upper plate of the subduction zone. Textural relationships and amphibole compositions in hornblendite indicate crystallization at lower crustal depths with pressures of 7-8 kbar in the Fuegian Batholith and of 5-6 kbar in the Ushuaia Pluton. Lower Cretaceous suites of hornblendite and calc-alkaline hornblende-gabbro, diorite and tonalite in the Fuegian Batholith have εNdt values ranging between +2 and +4. They were emplaced within an island arc coeval with mid-oceanic type spreading in the Rocas Verdes back-arc basin. Isotope ratios and amphibole compositions in hornblendite indicate crystallization from primitive and hydrous sub-alkaline basaltic melts with relatively low LREE/HREE and low alkali contents. The Late Cretaceous plutons in the fold-and-thrust belt were emplaced after the tectonic juxtaposition of Rocas Verdes ophiolitic complexes. The Ushuaia Pluton, consisting of clinopyroxene-hornblende cumulates, hornblende-gabbro, diorite and monzodiorite, was emplaced during the waning stage of Late Cretaceous magmatism. In this case hornblendite amphiboles show high contents of alkalis, LREE and incompatible elements with a strong crustal affinity (Th, Ba, Rb). The enriched incompatible trace element patterns indicate their derivation from K-rich transitional magmas formed in supra-subduction settings. Chemical variations in amphibole from hornblendites and spatially

related plutonic rocks are evaluated in terms of fluid flux from the subducted slab and partial melting of the sub-arc mantle, ultimately controlled by the thermal state of the subducted slab and convergence rates.

Keywords: Fuegian Batholith; Ushuaia Pluton; Cretaceous magmatism; Hornblendites; Amphibole; Rocas Verdes Basin

1. Introduction

Magmatism in convergent margins on Earth involves processes of partial melting of mantle lithosphere, crustal recycling, mountain building and volcanism. Magma evolution in Pacific-type magmatic arcs has been extensively studied on volcanic successions and composite batholiths, emplaced at different crustal depths. As lower crustal sections are rarely exposed, the origin of intermediate to silicic igneous rocks and the evolution of the continental crust is still debated. The andesite-dacite bulk composition of the continental crust cannot result directly from single-stage generation of mantle-derived magmas and requires processes such as differentiation of primary basaltic magmas by fractional crystallization within the uppermost mantle and lower crust (Gill, 1981; Grove and Kinzler, 1986; Hildreth and Moorbath, 1988; Müntener et al., 2001; Annen et al., 2006; Davidson et al., 2007) and partial melting of crustal rocks (e.g. Atherton and Petford, 1993; Chappell and White, 2001; Annen et al., 2006). The site of basalt injection and melt generation in the lower crust is thought of as a deep crustal hot zone where melts ultimately derive from the crystallization of mantle-derived basalts (residual melts) and partial melting of the lower continental crust (crustal melts). If melts are efficiently extracted within the magma batches in the lower continental crust, the residual mafic minerals will have a cumulate character, with associated high densities and seismic velocities (Debari and Coleman, 1989). The upward segregation of melts is accompanied by complex interplay of processes such as destabilization of magma batches, formation of "negative" cumulate diapirs and migration to shallow crustal depths (Cashman et al., 2017). Segregation of interstitial melt within a crystal mush can lead to its accumulation and formation of a new magma. The interconnected magma conduits and reservoirs, which store magma as it evolves into a crystal mush and is ultimately fed from a zone of partial

melting constitutes the magma plumbing system (Magee et al., 2018). Segregation of melt from lower crustal crystal mushes has been used to explain the extensive geochemical evidence for fractionation as a major process in the evolution of plutonic igneous rocks (Solano et al., 2012; Lee et al., 2014; Cashman et al., 2017; Edmonds et al., 2019). Differentiation in the lower arc crust may exert a dominant control on the geochemical and isotopic composition of magmas (e.g., Hildreth and Moorbath 1988; Davidson et al. 2007), whereas textural and petrographic aspects are predominantly acquired during shallow storage (e.g., Annen et al. 2006).

It is widely accepted that arc magmas can undergo significant modification at the base of the arc crust without leaving evidence in their mineral assemblages, due to cumulate–melt reaction, as seen in deep crustal sections worldwide (e.g., Debari & Coleman, 1989; Debari, 1997; Larocque and Canil, 2009, Tiepolo et al., 2011: 2012; Dessimoz et al. 2012; Nandedkar et al, 2016). Increasing attention has been paid to amphibole-rich cumulates, aiming to constrain the structural depth of differentiation processes within the arc crust (e.g., Müntener and Ulmer, 2006; Smith 2014). Additionally. Arc cumulates have the potential to record textural and chemical information from hidden and deep-seated crustal physicochemical processes in the first stages of magma differentiation. Nevertheless, there is a missing link regarding the diversity of magmatic processes between the chemical composition of cumulate assemblages and that of evolved plutonic rocks. Amphibole is one of the most important hydrous minerals in the middle and lower continental crust in arc settings. Its fractionation exerts a first-order effect on the formation of intermediate to silica-rich magmas (Sisson 1993; Hilyard et al. 2000; Müntener et al. 2001; Davidson et al. 2007; Nandedkar et al., 2016). The felsic average composition of extensive upper crustal batholiths suggests the existence of

_hidden' and deep-seated amphibole reservoirs (Davidson et al., 2007) represented by amphibole-rich mafic and ultramafic intrusive rocks (e.g. hornblendite, amphibole-gabbro and amphibole-diorite).

This study presents new petrographic, mineralogical, geochemical (whole-rock and in-situ major and trace elements), geochronological and isotope data on ultramafic, mafic and intermediate rocks from the Fuegian Batholith and Ushuaia Pluton, a rear-arc satellite pluton, in southernmost South America. Using new analyses of hornblendites, gabbros, granitoids and lamprophyres, we address the role played by amphibole (and other mafic phases) in the genesis of two distinct magmatic arcs formed during the late evolution of the Rocas Verdes back-arc basin following the tectonic emplacement of ophiolitic complexes (cf. Stern and de Wit, 2003; Klepeis et al., 2010; Calderón et al., 2012). The contrasting geochemical signatures are related to the origin of the hornblendites and their petrogenetic significance, providing insights into the structure of the magmatic plumbing systems in the Fuegian magmatic arc. It is shown that the trace element composition of amphibole can be used as a tracer of magmatic processes and as a proxy of the amount of H_2O-rich fluids involved in magma evolution.

2. Geological Setting

The Patagonian Batholith extends continuously along the continental margin of southern South America between 40ºS and 56ºS (Fig. 1). It represents the roots of a Mesozoic to Cenozoic magmatic arc built-up by episodically assembled calc-alkaline plutons (Hervé et al., 1984, 2007; Pankhurst et al., 1999). The crust into which the early plutons of the Patagonian Batholith were emplaced underwent regional extension linked to Gondwana break-

up from early Jurassic times (Pankhurst et al., 2000; Hervé et al., 2007; Dalziel et al., 2013). Lithospheric thinning along the southwestern continental margin resulted in the generation of silicic, mafic and bimodal magmatic suites linked to continental rifting and oceanic-type spreading in the overriding and attenuated continental crust (Bruhn et al., 1978; Hervé et al., 1981; Pankhurst et al., 2000; Stern and de Wit, 2003; Calderón et al., 2007a). Silicic volcanism is represented by subaqueous pyroclastic rocks and rhyolites of the Tobífera Formation, which unconformably overlie Paleozoic metamorphic complexes (Bruhn et al., 1978; Allen, 1982; Pankhurst et al., 2000; Calderón et al., 2007b, 2013).

Continuous extension in a supra-subduction setting triggered the development of the Late Jurassic–Early Cretaceous Rocas Verdes marginal basin and the formation of oceanic-type crust (Dalziel et al., 1974; Mukasa and Dalziel, 1996; Stern and de Wit, 2003; Calderón et al., 2007a, 2013). Remnants of the Rocas Verdes basin, from north to south, are represented by the Sarmiento, Capitán Aracena and Tortuga ophiolitic complexes (Fig. 1). Further to the south, the oceanic floor may have been linked to the opening of the Weddell Sea (de Wit, 1977; Grunow, 1993; Mukasa and Dalziel, 1996). The Rocas Verdes basin in-fill consists of Late Jurassic–Early Cretaceous hemipelagic sedimentary successions of the Yaghan and Zapata Formations (Katz and Watters, 1966; Dott et al., 1977; Suárez et al., 1981; Olivero and Malumián, 2008; Barbeau et al., 2009; Klepeis et al., 2010): they reach an estimated thickness of 3000–6000 m (Dott et al., 1977). The Rocas Verdes basin was bounded to the west by an Early Cretaceous magmatic arc (Calderón et al., 2007a). In the Fuegian Andes the products of this arc form the mainly intermediate and silicic volcanic and volcaniclastic rocks of the Hardy Formation (Suárez et al., 1985; Miller et al., 1994).

The Rocas Verdes basin started to close at the end of the Early Cretaceous (Aptian–Albian) (Halpern and Rex, 1972; Dalziel, 1981; Hervé et al., 1984; Cunningham, 1994),

involving underthrusting of its oceanic seafloor until Late Cretaceous time (Klepeis et al., 2010; Calderón et al., 2012) and post-tectonic lamprophyre emplacement. At the latitudes of the Fuegian Andes these processes culminated in the collision of the magmatic arcs and/or peripheral crustal block against the continent, as recorded in high-P and high-T metamorphic rocks of the Cordillera Darwin Metamorphic Complex (Nelson et al., 1978; Kohn et al., 1995; Klepeis et al., 2010; Maloney et al., 2011). Mid-Cretaceous crustal shortening was probably controlled by obduction at ~86 Ma and underthrusting of the South American continental crust at a pressure of ~12 kbar (Klepeis et al., 2010; Maloney et al., 2011). The Paleozoic basement and rift-related Jurassic volcanic and volcaniclastic rocks of the Cordillera Darwin Metamorphic Complex registered this phase of contraction (Klepeis et al., 2010; Hervé et al., 2010). The tectonic emplacement of ophiolites, tectonic loading and shortening marked the early development of the Magallanes–Austral foreland basin and of the Magallanes fold-and-thrust belt (Fildani et al., 2003; Ghiglione and Ramos, 2008; Romans et al., 2010; Fosdick et al., 2011; Torres Carbonell et al., 2017).

The southernmost segment of the Patagonian Batholith, south of the Magellan Strait and extending to the southern continental edge at 53–56ºS, is known as the Fuegian Batholith. Geochemical and spatial relationships along with available K-Ar mineral radiometric data allowed Hervé et al. (1984) to define three main plutonic groups: the Gabbro Complex (141 to 103 Ma), the Canal Beagle plutonic group (113 to 81 Ma) and the Seno Año Nuevo plutonic group (60 to 43 Ma). The emplacement of plutons belonging to the first two was in part coeval with closure of the Rocas Verdes Basin (Hervé et al., 1984; Klepeis et al., 2010); whereas rocks of the Tertiary Seno Año Nuevo plutonic group were intruded to the south of the Cretaceous Andean orogen (following a southward shift of the magmatic arc; Hervé et al., 1984) after a tectonothermal event related to inversion of the Rocas Verdes basin.

Satellite plutons located to the north of the Fuegian Batholith, such as the Santa Rosa and Castores plutons (ca. 92–81 Ma, K-Ar in hornblende and biotite; Suárez et al., 1986) in Isla Navarino and the Península Dumas pluton (ca. 85 Ma; Suárez et al., 1977), collectively known as the Beagle Channel Plutonic Complex. The whole-rock composition of granodiorites from Península Dumas indicates a high K calc-alkaline to calc-alkaline affinity (Suárez et al., 1977). Rear-arc plutonic rocks, located north of the Beagle Channel, are represented by isolated km-sized plutons, such as the Ushuaia, Moat, Kranck and Jeu-Jepén plutons: they range in age between 113 and 71 Ma (Acevedo et al., 2002; Peroni et al., 2009; González-Guillot et al., 2009, 2018). In northern latitudes (52–53ºS), migration of magmatism towards the continent has been related to progressive flattening of the subduction angle in mid-Cretaceous times (Stern et al., 1991).

3. Analytical Techniques

The U–Pb SHRIMP zircon ages determined for this investigation were obtained using SHRIMP II at RSES, ANU, Canberra. The measurement techniques employed followed those of Williams (1998) and Ireland et al. (2008). FC1 was used as the standard throughout and data were reduced using SQUID (Ludwig, 2001a) and Isoplot/Ex (Ludwig,2001).

Representative samples were selected for whole-rock geochemistry. Major and trace elements were analysed by inductively-coupled plasma mass-spectrometry at Activation Analytical Laboratories in Vancouver, Canada.

The Sr and Nd isotope determinations were carried out at Geochronological Research Center at the Universidade de São Paulo, Brazil, The rock powders (100 mg) were dissolved in Savillex beakers with HF and HNO_3 on a hot plate for 5 days at ~110 ^{o}C and were dried down

on a hot plate; the residue was dissolved in 6 M HCl at 110 ^{o}C for 24 hours. The HCl solution was dried down and concentrated HNO_3 was added on the residues. Samples were taken to dryness prior to re-dissolution for ion exchange purification. Sr was purified using Eichrom Sr-Spec® resin and eluted with 0.05 M HNO_3. Nd was purified using two steps of ion-exchange columns with RE-Spec® and LN-Spec®; Nd was eluted in 0.26 M HCl.

The Sr isotope ratios were determined on a Triton TIMS (thermo-ionization mass spectrometer) in dynamic mode. The ratios were normalized to $^{86}Sr/^{88}Sr = 0.1194$ and analysis for $^{87}Sr/^{86}Sr$ for the NBS987 standard during this study gave a mean value of 0.710250 ± 0.000018 (2σ). The Sr blanks were about 128 pg. The Nd isotope ratios were determined on aThermo Scientific Neptune multicollector ICP-MS. The ratios were normalized to $^{146}Nd/^{144}Nd = 0.7219$, and the $^{143}Nd/^{144}Nd$ average for the JNDi-1 standard during this study was 0.512197 ± 0.000004 (2σ). The analytical blanks were about 270 pg.

The major element compositions of amphibole from hornblendites, gabbros, granitoids and lamprophyres were determined at the Institut für Mineralogie und Kristallchemie, Universität Stuttgart, Germany, using a Cameca SX 100 electron microprobe. Operating conditions were set at 15 kV acceleration voltages and 15 nA beam current on both samples. Amphibole crystals were analysed *in situ* in polished thin sections.

Trace element mineral composition of amphibole was determined by laser-ablation inductively-coupled plasma mass-spectrometry (LA-ICPMS) at Institut für Mineralogie und Kristallchemie, Universität Stuttgart, Germany. For the LA-ICPMS measurements, an Agilent 7700 ICPMS was coupled to an LSX 213 laser equipment from Cetac (Ohio, Nebraska, USA). At 213 nm, the maximum laser energy is 4 mJ (pulse length < 5 ns) at a spot diameter of 200 microns. Laser excitation was carried out at an energy of 50% at a spot diameter of 50 microns

and a laser pulse frequency of 10 Hz. The data acquisition was performed using the Agilent Mass Hunter software (version B.01.01). Each analysis comprised the acquisition of background ion intensities (gas-blank) for roughly 25 s followed by the acquisition of the ion intensities on laser irradiation of the sample spot for roughly 60 s. Background-corrected individual ion intensities were integrated over a selected appropriate interval of the ablation time profile,. This integral was divided by the integral of the corrected intensity of the selected isotope of the internal reference element. The software used for calibration and data evaluation was developed by J. Opitz (Massonne et al., 2013).

DLH7 and DLH8 glasses from P&H Developments Ltd. and NIST612 and NIST610 glasses from National Institute of Standards and Technology, USA, were used as standards. Relative elemental concentrations were calculated from the abundance of the corresponding isotope assuming a natural isotopic distribution and an individual calibration factor which was determined under the same experimental conditions. The silicon elemental concentration, as calculated from the ^{29}Si isotope, was used as internal standard and set to the value obtained by EMPA.

4. Samples and petrography

Samples of gabbro, tonalite and hornblendite from the Fuegian Batholith and of monzodiorite and hornblendite from the Ushuaia Pluton were collected at different localities (Fig. 1). A sample of lamprophyre was collected from a metre-thick dyke cross-cutting the Tortuga ophiolite. Table 1 presents a summary of field relationships and descriptions of the different plutonic complexes in the Fuegian Batholith (Suárez et al., 1977, 1979; Hervé et al.,

1984) and of the Ushuaia Pluton (Acevedo et al., 2002; González-Guillot et al., 2018). Representative photomicrographs of the samples are illustrated in Figure 2.

4.1. Fuegian Batholith

Mafic and ultramafic rocks in the Fuegian Batholith have been grouped as a single gabbroic assemblage referred to as the Gabbro Complex, whereas tonalite is the main lithology of the Canal Beagle Plutonic Complex (Hervé et al., 1984). Gabbros belonging to the Seno Año Nuevo Plutonic Group (Paleogene) were also considered in the set of studied samples.

In the northeastern portion of the Isla Londonderry, hornblende gabbro and hornblendite are exposed as isolated outcrops and tonalite is the volumetrically most important lithology. The mafic and ultramafic bodies are mapped as ‗mega-inclusions` within the tonalite plutons (cf. Hervé et al., 1984), showing contact relationships that vary from sharp to gradational. The amphibole-rich cumulates vary from mid- to fine-grained hornblendite to pegmatitic hornblendite (Figs. 2a-b).

The medium-grained ´host´ tonalite (FC1854; Fig. 2c) in Isla Londonderry is composed of plagioclase (1–3mm), quartz (500 μm–2 mm), amphibole (1–4 mm), biotite (500 μm–1 mm) and accessory titanite (500–600 μm), Fe-Ti oxides (<400 μm), apatite (<400 μm) and zircon (<300 μm). Plagioclase is generally fresh with no visible zonation. Amphibole is more abundant than biotite, and both are partially chloritized. Titanite occurs as inclusions within amphibole, between grains or along fractures. Plagioclase from tonalite samples has an anorthite content of 45–53 mol %.

The hornblendite sample (13AP01-30; Fig. 2a) is mainly composed of mid- to fine-grained idiomorphic and equigranular hornblende (cumulus hornblende ranges from 1 to 3 mm and intercumulus hornblende crystals are <600 μm), occasionally skeletal, with minor inclusions of exsolved Fe-Ti oxides and interstitial anorthositic plagioclase (<600 μm). Amphibole crystals are randomly orientated and grain boundaries are commonly smooth, curvilinear and sutured. Euhedral hornblende displays orthocumulate texture with intercumulus plagioclase, suggesting high-temperature crystallization for the amphibole, prior to plagioclase. Neither reaction textures nor relicts are observed in this section. Accessory phases are disseminated granular magnetite–ilmenite pairs (<500 μm) that occur on the interfaces of plagioclase and amphibole, as well as inclusions on the edge of amphibole grains. Minor amounts of primary spinel (<400 μm) and secondary epidote (<350 μm) are also present.

The pegmatitic hornblendite dyke (13AP01-31; Fig. 2b), which cuts fine-grained hornblendites, is composed of idiomorphic coarse-grained amphibole (some up to 15 cm long) with fine-grained interstitial plagioclase (2–3 mm), magnetite–ilmenite pairs (<800 μm) with minor apatite, and late chlorite. Amphibole crystals are well preserved with elongated and crystallographically aligned exsolution lamellae of acicular rutile. Plagioclase is subhedral and partially replaced by fine-grained white mica.

On the northern shore of the Isla Thomas, dark plutonic rocks have been mapped as gabbroic rocks locally intruded by felsic plutons and late andesitic dykes (Suárez et al., 1985; Gómez et al., 2015). A medium-grained gabbro (AA1418; Fig. 2d) consists mainly of plagioclase (2–4 mm) and lesser amounts of amphibole (800 μm–2 mm) with relic inclusions of clinopyroxene, interstitial biotite (500–700 μm), magnetite (<400 μm), ilmenite (<400 μm),

sulfides and trace amounts of secondary epidote, chlorite and white mica. Amphibole is partially replaced by actinolite. A hornblende-biotite tonalite sample (AA1419) was collected from an ellipsoidal meter-sized late stage segregation body within the layered gabbros for U-Pb zircon geochronology to constrain the minimum crystallization age of mafic rocks.

A sample of fine- to medium-grained gabbro (FC1811; Fig. 2e) was collected from an isolated pluton intruding ophiolitic rocks in Hardy Peninsula (Seno Año Nuevo Plutonic Complex; Fig. 1). It is composed of plagioclase (800 μm–2 mm), clinopyroxene (500 μm–1 mm), amphibole (400 μm–1 mm), rare interstitial K-feldspar (400 μm), ilmenite (<350 μm), magnetite (<350 μm) and accessory apatite and zircon (<2 mm). The plagioclase does not show compositional zoning and the borders of clinopyroxene and amphibole are weakly replaced by actinolite and chlorite.

4.2. Ushuaia Pluton

The Ushuaia Pluton crops out immediately east of the city, along the northern coast of Beagle Channel (Fig. 1), and can be subdivided into two sections: an early ultramafic–mafic assemblage and a late-stage body composed mainly of monzodiorite and quartz-monzodiorite intruding the ultramafic section (González-Guillot et al., 2018). The ultramafic–mafic section forms a partly concentrically-zoned structure with a nucleus of hornblende pyroxenite and an envelope of hornblendite followed by an outermost zone of gabbro, diorite and quartz-diorite. There is a transition from hornblende pyroxenite through pyroxene hornblendite to hornblendite and then mingled hornblendite and gabbro, accompanied by a reduction in grain size (González-Guillot et al., 2018).

The studied hornblendite (MT289; Fig. 2g) is mainly composed of idiomorphic amphibole with Fe-Ti oxide inclusions. Plagioclase, titanite and magmatic epidote are minor constituents. Scarce relicts of clinopyroxene are observed in the core of some amphibole crystals. Amphibole replaces clinopyroxene along cracks and cleavage planes but also mantles clinopyroxene with less clear textural evidence for reaction-replacement. At the centre of some amphibole crystals subhedral remnants of a former mineral phase are observed that may be clinopyroxene completely replaced by chlorite. Amphibole crystals are generally arranged randomly and grain boundaries are commonly smooth, curviplanar and sutured with adcumulus texture. Coarse-grained hornblendites are mainly composed of idiomorphic amphibole and lesser amounts of apatite, Ti-magnetite and titanite, with secondary epidote and chlorite. Amphibole crystals are larger than 500 μm and up to 2 mm with inclusions of plagioclase (<350 μm), opaque minerals (<300 μm), occasional clinopyroxene and apatite. Plagioclase is rarely observed as inclusions in amphibole and K-feldspar (<300 μm) is restricted to interstitial sites. Phlogopite, primary epidote and plagioclase are present in some specimens.

The medium-grained monzodiorite (MT112; Fig. 2h) consists of amphibole (2–3 mm), plagioclase (500 μm–2 mm), titanite (1 mm) with minor K-feldspar (500–600 μm), zircon (<250 μm) and opaque minerals (<400 μm). Hornblende is abundant and partially chloritized. Plagioclase is unzoned and partly replaced by white mica. Subhedral titanite crystals are isolated and K-feldspar is a minor and interstitial constituent. Other monzodiorites of the suite contain clinopyroxene and minor biotite (González-Guillot et al., 2018).

4.3. Lamprophyre

In Isla Navarino (Fig. 1) the Tortuga Ophiolitic Complex is intruded by plutons of 100–80 Ma belonging to the Canal Beagle Plutonic Group (Hervé et al., 1984) cropping out north of the Fuegian Batholith. The fine-grained spessartitic lamprophyre sample (TN0713C; Fig. 2f) was collected from a metre-thick dyke intruding pillow basalts. It displays microporphyritic texture with phenocrysts of amphibole (1 mm), clinopyroxene (<600 μm) and chlorite pseudomorphs after olivine. Amphibole crystals are euhedral and often weakly zoned. The groundmass (<600 μm) consists of plagioclase, amphibole, chlorite pseudomorphs, opaque minerals and secondary actinolite, epidote and titanite.

5. Geochronology

Previous geochronological studies in the northeast portion of Isla Londonderry by Hervé et al. (1984) presented K-Ar data for primary amphibole in gabbro (Gabbro Complex) and biotite in tonalite (Canal Beagle Plutonic Complex), yielding ages of ca. 130 Ma and ca. 109 Ma, respectively. Poblete et al. (2015) determined an amphibole $^{40}Ar/^{39}Ar$ plateau age of 102.0 ± 0.4 Ma for hornblendite.

Hornblendites in the Ushuaia Pluton have been dated by K-Ar whole rock analysis yielding an age of 113 ± 5 Ma (Acevedo et al., 2002) and 102 ± 3 Ma (Peroni et al., 2009). However, González-Guillot et al. (2018), using LA–ICP–MS U–Pb dating of zircons from a gabbro segregation contained in the hornblende pyroxenite and a monzodiorite, yielded

average ages of 75.0 ± 1.0 and 74.0 ± 0.4 Ma, respectively, which they interpreted as the emplacement and crystallization age of the Ushuaia Pluton.

We present new U–Pb zircon ages for a tonalite and two gabbros from the Fuegian Batholith (Table 2). The new results and representative age probability plots for individual samples are shown (Fig. 3).

Thirty zircon grains from the amphibole–biotite tonalite from Isla Londonderry (FC1854**)**, located near the contact with the mega-inclusion of gabbros and hornblendites, were analysed. Crystals are elongated and mixed with rhomboidal crystals with bi-pyramidal terminations, many multifaceted. Zoning parallel to the length of the crystals can be distinguished, as well as sector zoning. The U-Pb determinations yielded a dominant crystallization age of 122 ± 1 Ma (MSWD = 1.19, Fig. 3a).

Based on field, mineralogical and geochemical data, the sigmoidal segregation of tonalite (AA1419) within layered amphibole gabbros in Isla Thomas has been interpreted as a late magmatic product during the crystallization of the gabbros (Gómez, 2015). Twenty-six zircon grains were analysed from this sample. Zircon crystals are 100–300 μm long, pseudo–prismatic and elongated to equidimensional. We distinguished igneous structures characteristic of mafic igneous zircons: wide to weak zonation, sectorized zones or wide zones parallel to the length of the crystal. A few grains are subrounded, suggesting incipient resorption during interaction with the host magma. The U-Pb determinations yielded a weighted mean of 123 ± 1 Ma (MSWD 1.5; Fig. 3b), which is interpreted as the crystallization age of the tonalite and considered representative of the (minimum) age of the host gabbro.

Twenty-six zircon grains from the clinopyroxene-hornblende gabbro (FC1811) located on Hardy Peninsula were analysed. U-Pb measurements in twenty-nine spots yielded a

weighted mean age of 60.5 ± 0.6 Ma (MSWD 1.07; Fig. 3c), which is interpreted as the crystallization age.

6. Whole-rock geochemistry

6.1 Major elements

The bulk rock geochemical compositions are presented in Table 3. Data for the Fuegian Batholith follow a calc-alkaline trend, ranging in composition from gabbro to granodiorite, as in Hervé et al. (1984). Jurassic granites in Cordillera Darwin (Hervé et al., 1981, 2010; Klepeis et al., 2010), outside the limits of the Fuegian Batholith, were formed during the rifting stage of the Rocas Verdes basin formation. The geochemical data for the Ushuaia Pluton (Acevedo et al.,2002; González-Guillot et al. 2018) indicate that monzodiorites and minor quartz-monzodiorites plot in the transitional field between high–K calc-alkaline and alkaline magma series (González-Guillot, 2016).

6.2 REE and incompatible elements

The chondrite–normalized pattern of Rare Earth Elements (REE; Fig. 4a) in hornblendites from the Fuegian Batholith is convex upward with enrichment in middle-REE (MREE) relative to light-REE (LREE) and heavy-REE (HREE), as expected for a rock composed of >90% hornblende, which has a partition coefficient consistent with this pattern (e.g. Tiepolo et al., 2007; Nandedkar et al., 2014). No Eu anomaly is observed, consistent with late crystallization of plagioclase.

The REE pattern of the Aptian tonalite in the Fuegian Batholith (FC1854) is flat and shows minor enrichment in LREE relative to MREE and HREE, with no Eu anomaly (Fig. 4c). Incompatible trace elements show enrichment in LILE, negligible Nb-Ta and Ti anomalies, a positive Pb anomaly and low Ba contents (Fig.4b). The gabbros display essentially flat REE patterns with positive Eu anomalies, indicating plagioclase accumulation. The multi-element pattern of the Aptian hornblende-clinopyroxene gabbro (AA1418; Fig.4b) shows depletion in LILE, with slight Nb-Ta depletion and a positive Pb anomaly. In contrast, the Paleocene hornblende-clinopyroxene gabbro (FC1811) shows enrichment in LILE, a negative Nb-Ta anomaly and low contents of Eu and Ti (Fig. 4d).

Monzodiorite from Ushuaia Pluton shows a slightly convex REE pattern with enrichment in LREE relative to HREE and no Eu anomaly (Fig. 4e).

The chondrite-normalized REE pattern of the lamprophyre sample displays a marked enrichment of LREE relative to MREE and HREE, with no Eu anomaly (Fig. 4f). The incompatible trace element pattern shows enrichment in LILE with a Nb-Ta anomaly and slight Ti depletion.

6.3 Sr-Nd isotopic composition

Sr and Nd data for samples from the Fuegian Batholith data are reported in Table 4 and shown in Figure 5. The isotopic composition of hornblendites and tonalites from the Fuegian Batholith was recalculated at 120 Ma. The hornblendite (hb) and pegmatitic hornblendite (p-hb) have initial $^{87}Sr/^{86}Sr$ ratios of 0.7040 and 0.7039 and positive εNd_t values of +1.9 and +3.7, respectively. The two tonalites have similar initial $^{87}Sr/^{86}Sr$ ratios of 0.7039 and positive

εNd values of +3.1. The Paleocene hornblende gabbro has initial $^{87}Sr/^{86}Sr$ ratios of 0.7037 and εNd of +5.0. These isotopic signatures signify the primitive origin of precursor magmas, derived from a sub-arc mantle source. The data plot in the same field as those of Cretaceous tonalites and granodiorites from the South Patagonian Batholith (cf. Hervé et al., 2007).

7. Amphibole composition

The major and trace element composition of amphibole from the studied samples is reported in Tables 5 and 6 respectively.

7.1 Hornblendites

The hornblendite from the Fuegian Batholith (13AP01-30) consists of amphibole crystals with a relatively homogenous major element composition: they are magnesium-rich (Mg>Fe) and Al–rich (11–13 wt.% Al_2O_3) calcic amphiboles. Following the nomenclature of Leake et al. (1997) the composition is mainly magnesio-hastingsite ($^{VI}Al < Fe^{+3}$) with slight variations to tschermakitic hornblende and pargasite (Fig. 6). These amphiboles are mainly characterized by Mg# ~0.71, Al_{tot} ~2.57 a.p.f.u., alkali content (Na+K) in the range 0.59–0.72 a.p.f.u and Ti content up to 0.19 a.p.f.u. The Cr and Ni contents are up to 112 and 29 ppm. The chondrite-normalized REE patterns show depletion of LREE (La_N/Sm_N= 0.15–0.27) and HREE (Gd_N/Yb_N= 1.54–1.93) relative to MREE (Fig. 6a). No significant Eu anomaly is observed, indicating that amphibole crystallized prior to plagioclase. A multi-element trace pattern reveals depletion in Nb and positive anomalies in Sr, Zr and Ti, relative to elements with similar incompatibility: however, these anomalies correspond to an extremely low concentration of REE rather than an enrichment in those elements. In this rock plagioclase is

interstitial and is almost pure anorthite (An_{87-98}). The lack of chemical zonation suggests fast cooling or re-equilibration at high temperature.

The composition of hornblende from the Ushuaia Pluton hornblendite (MT289) varies from magnesio-hastingsite ($^{VI}Al < Fe^{+3}$) to pargasite ($^{VI}Al > Fe^{+3}$). These amphiboles are relatively similar to those in the Fuegian Batholith, with Ti contents, up to 0.22 a.p.f.u., slightly lower Mg# with values of ~0.64, in the same range as amphibole in other hornblendites from the Ushuaia Pluton (Mg# of 0.65–0.58; Acevedo et al., 2002), and Al_{tot} content around 2.36 a.p.f.u. Alkali content (Na + K) ranges from 0.93 to 1.01 a.p.f.u., the most notable difference from the Fuegian Batholith amphiboles in terms of major elements. Rim compositions vary slightly, being more enriched in LREE. The Ni contents are comparable to magnesio-hastingsite in the hornblendite of the Fuegian Batholith (29–35 ppm), but the Cr contents are considerably lower (up to 32 ppm). Another common feature between the magnesio-hastingsite of hornblendites in the Fuegian Batholith and Ushuaia pluton, compared to the hornblende from gabbros and granitoids, is the higher Sr content relative to LREE (Sr/Nd>20 in hornblendites and Sr/Nd<5 in gabbros and granitoids) and their high Eu/Eu* ratios (>0.8). However, despite these similarities, the trace element signature is substantially different from that of amphiboles in the Fuegian Batholith, showing LREE enrichment relative to MREE (La_N/Sm_N= 0.58–1.43). LREE concentrations in amphibole from the Ushuaia Pluton are almost three times those from the Fuegian Batholith. Multi-element patterns show depletion in Nb, Zr and Ti relative to other elements.

7.2 Gabbros and granitoids

The amphibole in gabbros is magnesio-hornblende, with higher Mg# and lower Eu/Eu* than those in the hornblendites. The Mg# of ~0.75 in the Aptian Gabbro of Isla Thomas (AA1418) is slightly lower than for the Paleocene gabbro (FC1811) with an average of ~0.79. Amphiboles are characterized by Ti contents of 0.05 (AA1418) and 0.22 a.p.f.u. (FC1811), with average Al_{tot} values up to 1.0 and 1.2 a.p.f.u., respectively. The chondrite-normalized REE pattern varies from convex upward to flat (Fig. 7b). Amphibole in the Aptian gabbro shows a marked depletion in LREE (La_N/Yb_N=0.16–0.27) and enrichment in MREE with a negative Eu anomaly (Fig. 7b). The incompatible trace element diagram displays depletion in Nb, Sr, Zr and Ti relative to REE for both gabbros, but this is more pronounced in AA1418. The Ni and Cr are 27 and 59 ppm, respectively, for the Aptian gabbro, and 2 and 26 ppm, respectively, for the Paleogene gabbro.

In the Aptian tonalite (FC1854) of Isla Londonderry, the amphibole is mainly magnesio-hornblende and minor edenite. It has low Ti contents, up to 0.11 a.p.f.u., along with an average Al_{tot} value of 1.76 a.p.f.u. The average Mg# value is 0.63. The chondrite-normalized pattern varies from flat to slightly convex upward with a negative Eu anomaly and a slight depletion in LREE (La_N/Sm_N= 0.25–0.41) relative to MREE and HREE (Fig. 7c). The incompatible trace element pattern reveals depletion in Sr, Zr and Ti relative to REE. The Cr and Ni contents are 21 and 23 ppm, respectively.

Amphibole in the Campanian monzodiorite (MT112) from the Ushuaia Pluton is mainly hastingsite ($^{VI}Al<Fe^{+3}$) but edenite, ferro-edenite, magnesio-hornblende and ferro-hornblende compositions are also identified. The average Mg# value is 0.48. Amphibole in monzodiorite is characterized by Ti contents up to 0.2 a.p.f.u, Al_{tot} averages 1.94 a.p.f.u. and

alkali contents range from 0.5 to 0.8 a.p.f.u. Among all the studied samples, this is the only one whose amphibole has a concave upward chondrite-normalized pattern (Dy/Dy*<1) that exhibits LREE enrichment relative to MREE and HREE (Fig. 7c). The incompatible trace element pattern reveals depletion in Sr and Zr. The Cr content has an average value of 10 ppm. The Ni contents are comparable with those of the tonalite samples from the Fuegian Batholith (23 ppm).

7.3 Lamprophyre

The major element composition of euhedral amphibole phenocrysts in the Cenomanian lamprophyre (TN0713C) is relatively homogeneous and of similar composition to amphibole in the groundmass. Amphibole phenocrysts are mainly magnesio-hastingsite although pargasite, tschermakitic hornblende and magnesio-hornblende compositions are also measured. The Cr and Ni contents (up to 1640 and 254 ppm, respectively) and the Mg# (average ~0.87) are the highest of all the studied samples. The Ti content is up to 0.25 a.p.f.u. and Al_{tot} is up to 2.49 a.p.f.u. The alkali content ranges from 0.47 to 0.82 a.p.f.u. The chondrite-normalized REE pattern displays MREE enrichment relative to HREE and LREE and a negligible negative Eu anomaly (Fig. 8d). The multi-element trace elements pattern displays enrichment in Ba and Sr and depletion in Zr relative to other elements.

8. Discussion

8.1. Thermobarometry

The study of mafic and ultramafic cumulates in Andean-type batholiths can be used to constrain the structural depth of pluton emplacement and differentiation within magmatic arcs (e.g. Müntener and Ulmer, 2006). Generally, the emplacement depth of plutons is rather difficult to constrain due to the lack of appropriate number of phases in the mineral assemblages for geobarometry. However, the mineralogy of the amphibole-rich cumulates can potentially be used to constrain the minimum temperature for crystallization and to quantify the depths at which subsolidus reactions occurred (cf. Yavuz and Döner, 2017). Although the total Al_2O_3 content of amphibole is mainly dependent on melt composition and temperature, the Al^{VI} content has a significant pressure dependency (e.g., Holloway and Burnham 1972; Putirka 2016). The single amphibole barometer of Ridolfi et al. (2010) would be suitable for the hornblendite samples, but we do not use this because of concerns raised by Erdmann et al. (2014) and Putirka (2016). Experiments conducted in basalts with high Mg-numbers at various pressure conditions provide a correlation between pressure and Al^{VI} in hornblende that can be used as an empirical barometer (Larocque and Canil, 2009). A recalibration was suggested by Krawczynki et al. (2012) based on a wider range of bulk rock compositions. Temperature was calculated using Putirka's (2016) pressure-independent thermometer (Equation 5) based on Si, Ti, Na and Fe contents with an uncertainty of ± 30°C . In the case of tonalite and granodiorite, the geobarometers that use Al^{VI} in hornblende (e.g. Ridolfi et al., 2010) did not give consistent results with the rest of the classic geobarometers, so we estimate the depth of crystallization using experimental and empirical amphibole geobarometers based on the Al^{tot} content, derived from the structural formula of amphibole (Hammarstrom and Zen, 1986; Hollister et al., 1987; Johnson and Rutherford, 1989; Schmidt, 1992).

In the studied hornblendites, the average estimates of the pressure for amphibole crystallization is 7–8 kbar in the Fuegian Batholith and 5-6 kbar in the Ushuaia Pluton. The

thermometers yield temperatures ranging between 980 and 1010 ºC and between 945 and 970 ºC, respectively. Pressure estimations by González Guillot et al. (2018) also range between 5 and 7 kbar for the hornblendite in Ushuaia Pluton. The average hornblende-derived pressure of crystallization for the Aptian tonalite (FC1854) is ca. 5 kbar at a temperature of 700 ºC, reflecting near-solidus chemical re-equilibration. The average pressure for hornblende crystallization in the monzodiorite of the Ushuaia Pluton is ca. 3 kbar.

According to P–T constraints in the hornblendite from the Fuegian Batholith, amphibole crystallization occurred around 7–8 kbar, approximately at 25–30 km depth. This corresponds to the lower arc crust, roughly the crustal thickness in the Fuegian Batholith during mid-Cretaceous. Geothermobarometric constraints are consistent with experimental studies and the occurrence of Mg–rich amphibole with high Al^{VI} content (Fig. 8b) in similar amphibole–bearing ultramafic cumulates in other lower crustal sections (Himmelberg and Loney, 1995; Müntener and Ulmer, 2006; Larocque and Canil, 2009; Tiepolo et al., 2011; Dessimoz et al., 2012; Blatter et al., 2013; Nandedkar et al., 2014; Melekhova et al., 2015), but such results have not been previously found in Patagonian arc cumulates. The late emplacement of large tonalite magma batches in intermediate magma storage systems, as suggested by subsolidus re-equilibration of amphibole in the analysed Aptian tonalite (at ca. 5 kbar; approximately 15 km depth), suggests that hornblendites were exhumed by as much as 3–6 km from their initial position, by means of volcanic arc erosion, tectonism and magmatic underplating.

8.2. Petrogenesis of hornblendites and granitoids

The amphibole composition is relevant to identifying the magmatic processes active during the emplacement of the Fuegian Batholith and Ushuaia Pluton. In the following paragraphs, discussion will be centered on the hornblendite–tonalite and hornblendite–monzodiorite suites recognized in the batholith and in the Fuegian fold-and-thrust belt. It will be assumed that: (i) clinopyroxene, a near-ubiquitous mineral in arc magmas, can crystallize independent of initial water content, unlike orthopyroxene (Bonechi et al., 2017); the early stage of clinopyroxene (and olivine) fractionation would result in the bulk decrease of Mg# of late mafic phases, an increase of the alkali content and H_2O content in residual melts, and amphibole crystallization in a basaltic melt at near constant SiO_2 content.

(ii) plagioclase fractionation in precursor basaltic melts can be suppressed by high H_2O contents and/or depth of magma evolution (cf. Baker and Eggler, 1983; Sisson and Grove 1993; Müntener et al. 2001; Kelemen et al., 2003; Müntener and Ulmer 2006; Pichavant and Macdonald 2007; Nandedkar et al. 2014; Melekhova et al. 2015).

Cumulate rocks are strictly igneous in origin, but their bulk compositions do not represent the composition of original melts from which they crystallized (Cox, 1979). Nevertheless several features of those magmas can be interpreted from the textural and geochemical signatures of cumulate minerals. While cumulates are forming, the interstitial melt remaining in the crystal mush will be depleted in those elements incorporated into the structure of amphibole and/or other mafic phases. Depending on the rates of undercooling of interstitial melts, these will crystallize to form late intercumulus phases, or could interact and modify the early-formed cumulus crystals. The orthocumulate texture of hornblendites and plagioclase-rich hornblendites from the Fuegian Batholith, with interstitial Ca-rich plagioclase and subordinate amounts of spinel and magnetite-ilmenite pairs, was formed from rapid undercooling of intercumulus melt trapped within magnesio-hastingsite crystal mush.

Conversely, adcumulate texture and the trace element composition of core and rims in amphibole of hornblendites from the Ushuaia Pluton indicate re-equilibration between amphibole and the intercumulus liquid, resulting in late growth of cumulus grains of different composition. Complexities arise when considering that these processes would have been accompanied by late extraction and segregation of intercumulus melts into the adjacent magma reservoir, or melt infiltration from the magma reservoir or country rocks.

In the Fuegian Batholith, we interpret plagioclase-hornblendites as the result of progressive fractional crystallization of a primitive, hydrous sub-alkaline basaltic melt, constituting a high-pressure (7–8 Kbar) hydrous crystallization trend. Due to the lack of other mafic phases, it is assumed that amphibole either formed by a peritectic reaction consuming clinopyroxene, leaving no trace/relict, or that it crystallized directly from the melt. In either case, early and cryptic crystallization of clinopyroxene and/or olivine in earlier magmatic reservoirs cannot be discarded. The early stabilization of amphibole is reflected by the combination of high Mg# (0.71) and Al^{VI} which indicates crystallization at lower crustal pressures. Magnesio–hastingsite and pargasite, present in hornblendites and monzodiorites of the Ushuaia Pluton and Fuegian Batholith, have been reported in different arc root complexes (Tiepolo et al., 2011; Tiepolo et al., 2011; Larocque and Canil, 2010; Dessimoz et al., 2012) and are considered as "early" phases formed at high temperatures with low Si content and high (Na+K) content (Fig. 8a). By contrast, the magnesio–hornblende composition of amphibole in gabbros and tonalites of the Fuegian Batholith can be assigned to "late" phases, restricted to the low temperature consolidation of magma batches. Estimated crystallization temperatures for amphibole with >1.5 wt. % TiO_2 are consistent with those of amphiboles in primary hydrous magmas (Molina et al., 2009). This, along with textural evidence, also supports the early (high temperature) character of magnesio–hastingsite and pargasite from hornblendites.

They display high Mg# and Eu/Eu* values ranging between 0.8 and 1.0 (Fig. 8b-c-d) indicating negligible plagioclase fractionation in the early stages of magma evolution. The trace element compositions of amphibole indicate that the primitive magma had relatively low LREE contents. The low LREE abundances in the whole rock and amphibole from gabbros and tonalites (Figs. 4 b-c) are probably linked to high degrees of partial melting of the mantle source beneath an island arc (e.g., >20% partial melting of a mantle source with more than 0.2 wt.% H_2O; cf. Kushiro, 2007) or depletion processes by melt extraction in the sub-continental lithospheric mantle.

The low La/Sm values and Eu/Eu* of ~ 0.8–1.0 in hornblendite amphiboles suggest crystallization prior to plagioclase in early sub-alkaline hydrous basaltic magmas with high H_2O content (> 3 wt.%; cf. Müntener, 2001). The increase of La/Sm values recorded in the tonalite amphibole is accompanied by a decrease in Mg# and Eu/Eu* values, indicating crystallization after plagioclase and early amphibole (and/or clinopyroxene), in the middle section of the crust-scale magmatic column. Late amphibole in gabbros of the Fuegian Batholith, with high Mg# (~0.7-0.8) and Eu/Eu* of ~0.5-0.7 (Fig. 9 b-d), also crystallized after plagioclase and clinopyroxene fractionation, at the site of pluton emplacement and by interaction between clinopyroxene and intergranular basaltic melts with relatively high H_2O content.

Conversely, in the Ushuaia Pluton, cumulates form a compositional and textural continuum from hornblende pyroxenite through pyroxene hornblendite to pure hornblendite and an outer zone of mingled hornblendite and gabbro/diorite (González Guillot et al., 2018). Hornblendite reflects the early crystallization of anhydrous mafic phases in crystal mushes, as indicated by the low Mg-number (Mg#~63). Clinopyroxene is replaced by amphibole along cleavage planes and rims. Subhedral clinopyroxene inclusions in amphibole suggest that

residual melts did not strongly interact with early mafic phases and amphibole crystallization proceded once the H_2O content in the melt was higher than 3 wt.%. It is thus envisaged that hornblendite crystallized from hydrous residual melts locally distributed in the margins and/or magmatic conduits of the Ushuaia Pluton.

Amphiboles from hornblendite in the Ushuaia Pluton show higher contents of alkalis, LREE and incompatible elements with a strong crustal affinity (Th, Ba, Rb), which reflects crystallization from more enriched residual melts established after the early-stage crystallization of clinopyroxene-rich mushes. Furthermore, the difference of trace element abundances between the two analysed grains in this hornblendite reflects cryptic stages of amphibole crystallization (Figs. 7-8a), with a more enriched composition in the outer rims of crystals. Although melts derived from younger magma injections or partial melts derived from the host rock could also have infiltrated the mush, we consider that this possibility is less likely given the small size of the Ushuaia Pluton (emplaced probably in a time span of 100 ka). This is also supported by the high rate of magma injection proposed for pluton emplacement based on local textural evidence of incomplete consolidation of magma batches (González Guillot et al., 2018).

The low Dy/Dy* and high Dy/Yb values in hornblendites (Fig. 8e) allow us to infer the presence of sedimentary components in a metasomatized mantle source (cf. Davidson et al., 2012). The crystal mushes were emplaced at shallow levels of the crust within the Fuegian fold-and-thrust belt and continued to differentiate with the segregation of residual melts. The increase of La/Sm values in amphibole from hornblendite to monzodiorite in the Ushuaia Pluton, at nearly constant values Eu/Eu* (of~ 0.8-1.0), indicate that suppression of plagioclase fractionation and the high-H_2O content of residual magmas persisted until the crystallization of monzodiorites.

There are similar trace element abundances in amphibole of the Ushuaia Pluton hornblendite and the lamprophyre dyke. High Mg# (of ca.85–90) and high contents of Cr and Ni of lamprophyre indicates that the magmas were initially equilibrated with the mantle source, without being significantly affected by fractional crystallization or crustal contamination during ascent. We tentatively suggest the lamprophyres as likely candidates to represent the precursor mantle-derived hydrous basaltic melts of the rear-arc satellite plutons; this could explain the high contents of (Na+K) and LREE and negligible Eu anomalies in the Ushuaia Pluton amphiboles (Figs. 7a and d). This is also supported by the occurrence of lamprophyres dykes within the ophiolites and plutons of the Fuegian fold-and-thrust belt, emplaced after the tectonic emplacement of the Rocas Verdes ophiolitic complexes.

8.3. Geodynamic and magmatic evolution

Hornblende-rich cumulates and spatially associated gabbroic and granitoid rocks of the Fuegian Batholith and Ushuaia Pluton provide constraints on the origin of precursor primary basaltic magmas and on the partial melting degree of the mantle source. The trace element composition of amphibole in the suite of studied samples, with distinctive negative Nb and Ti anomalies (Fig. 7), support their origin in the upper plate of a subduction zone, as previously indicated by bulk-rock chemical affinities with magmatic arc products (Fig. 4; Hervé et al. 1984; González Guillot et al., 2018). Plutonic rocks of the Fuegian Batholith show calc-alkaline affinities, whereas those of the Fuegian fold-and-thrust belt have been classified as mildly alkaline or transitional (Gonzalez Guillot et al. 2009, 2018), formed at greater distances from the oceanic trench than the calc-alkaline suites (Morrison, 1980). In particular, the amphibole chemistry of the Ushuaia Pluton shows calc-alkaline indications but their enriched

incompatible trace element patterns distinguish them from those of typical arc magmas, rather suggesting a K-rich transitional type. Here, it is emphasized the key petrological significance of hornblendites that provide a glimpse of the earliest stages of magmatic differentiation and record the multi-stage evolutionary process at different crustal depths. According to available geochronological data and the geographical position of the Ushuaia Pluton and lamprophyres to the north and outside the limits of the Fuegian Batholith, it is considered that Cretaceous magmatism, between 125 and 65 Ma, occurred in two different magmatic arcs during the tectonic evolution of the proto-margin of Patagonia.

The Aptian magmatic arc, represented by calc-alkaline gabbro-tonalite-granodiorite suites and amphibole-rich cumulates in the Fuegian Batholith (Hervé et al., 1984), was contemporaneous with steep subduction of the oceanic slab and oceanic-spreading in the Rocas Verdes Basin. As for mature island arcs in subduction settings, the primary magmas probably originated as high-degree melts (>20%) of mantle sources, as suggested by flat REE patterns in whole rocks. The Nd isotopic signature in tonalites and hornblendites (εNd: +1.9 to +3.7; Fig. 5) verifies the primitive origin of precursor magmas derived from an enriched sub-arc mantle source, variably metasomatized by slab- or crustal-derived components. The late amphibole of the gabbros, formed after plagioclase and clinopyroxene fractionation, indicates lower contents of H_2O in the precursor basaltic magmas. The high Mg# (~0.7-0.8) of amphiboles suggests minor fractionation of olivine and clinopyroxene in the lower arc crust (Fig. 9).

Hornblendites were generated from magmas with high H_2O contents (>3 wt.%) that stabilized at lower crustal depths (approximately 25–30 km) within the island arc. The subtle negative Eu anomaly in amphiboles indicates that amphibole fractionation was in part coeval with late interstitial plagioclase. The amphibole in the tonalite, with La/Yb ~ 2.0 and without

Eu anomaly, was derived from residual melts generated after the fractionational crytallization of olivine, clinopyroxene and plagioclase at lower crustal depths. Evolved magmas were segregated and ascended to the middle crust (~15 km) where they stalled and crystallized as tonalites. The more evolved plutonic rocks of the Fuegian Batholith (tonalites and granodiorites), which are volumetrically dominant, may have crystallized in the middle crust within a melt–rich layer (or magma chamber) several hundreds of metres thick, leaving behind a thick melt-poor cumulate pile of gabbroic rocks and hornblendites.

The construction of the Upper Cretaceous magmatic arc started after the closure of the Rocas Verdes basin and early tectonic emplacement of ophiolitic complexes. The early phase of basin inversion was related to changes in subduction parameters along the continental margin of southernmost South America, linked to rapid spreading in the southern Atlantic Ocean and fast convergence rates of the proto-Pacific oceanic lithosphere (Dalziel, 1990; Stern et al., 1991).

The Upper Cretaceous plutons are mainly located to the north and outside the margins of the Fuegian Batholith, such as the Castores and Santa Rosa plutons in Isla Navarino (Fig. 1), together with the Ushuaia Pluton and similar bodies in the Fuegian fold-and-thrust belt. Their geographic location suggests a northeastward migration of the subduction-related magmatism that began in the mid-Cretaceous, related to the flattening of the subducted oceanic slab of the proto-Pacific Ocean (Stern et al., 1991; de Wit, 1997; Gonzalez Guillot et al., 2011). In this scenario, we propose that slab-derived fluid flux into the mantle source decreased with time and thus the degree of partial melting also diminished. Low melting degrees favored the generation of primitive magmas with high contents of H_2O (> 3 wt.%), Mg, (Na + K) and LREE similar to those resulting in lamprophyres.

The origin of the major enrichment in LILE and LREE, along with a depletion in Nb-

Ta-Ti as observed in hornblendites and late-stage monzodiorite suite from Ushuaia Pluton, could be derived from subduction-related metasomatism in the lithospheric mantle (e.g., Pearce and Peate, 1995; Turner, 2005; Altherr et al., 2008; Boari et al., 2009). Additionally, the slight depletion in High Field Strength Elements (HFSE) may be attributed to the retention of these elements in the subducting slab during progressive dehydration, whereas the LILE and LREE were transported upwards by slab-derived fluids, melts and or recycled sediments (Hawkesworth et al., 1993; M nker et al., 2004). It has been suggested that the transitional late-stage monzodiorite suites are the result of AFC (combined assimilation and fractionation) processes and incorporation of sedimentary material during the ascent of magmas (Gonzalez Guillot et al., 2009), as evidenced by metasedimentary xenoliths. Additionally, the wide range of Nd isotopic compositions in plutons of the Fuegian fold-and-thrust belt (such as the Moat Pluton with εNd +4.3 to -1.4; Gonzalez Guillot et al., 2009), probably reflects partial assimilation of supra-crustal components during ascent and emplacement. However, the incorporation of sediments and metasomatism of the mantle source cannot be ruled out, as suggested by low Dy/Dy* and high Dy/Yb values in hornblendite amphibole of the Ushuaia Pluton (Fig. 8e).

The protracted evolution of the Aptian and Upper Cretaceous arcs culminated with the emplacement of Paleogene plutons to the south, in the main axis of the Fuegian Batholith (Fig. 1b), interpreted as reflecting the southward migration of the magmatic loci (Hervé et al., 1984).

9. Concluding remarks

The comprehensive geochemical study of amphibole from Cretaceous hornblendites, gabbros and tonalites of the Fuegian Batholith and hornblendites and monzodiorites of the Ushuaia Pluton, provides insights into the complex magmatic evolution of two distinct magmatic arcs of the Fuegian Andes developed during the tectonic evolution of the Rocas Verdes Basin. The main conclusions that can be drawn from this study are:

1. The contrasting geochemical characteristics of plutonic rocks and amphibole in the Fuegian Batholith and Ushuaia Pluton were controlled by changes in the subduction parameters and thermal state of the subducted slab, which ultimately controlled fluid–flux from the slab and the partial melting degree of the sub-arc mantle. More detailed and systematic isotopic studies would be necessary to evaluate the role of recycled sediment in the mantle source of magmas.
2. The Lower Cretaceous plutonic rocks of the Fuegian Batholith, formed during the extensional phase of the Rocas Verdes Basin (steep subduction), record the early fractionation of mafic phases and accumulation in deep crustal magma reservoirs above subduction zones. Textural and geochemical constraints support a primary origin for magnesio–hastingsite and pargasite from hornblendites that crystallized from primary sub-alkaline hydrous melts.
3. The Upper Cretaceous Ushuaia Pluton, formed after the tectonic emplacement of the Rocas Verdes Basin ophiolites (flat subduction), record the evolution from clinopyroxene hornblendites and hornblendites to amphibole-bearing gabbros and monzodiorites. Although most amphibole in hornblendites crystallized from primary magmas some may have formed at the expense of clinopyroxene. Minor enrichment in LREE and incompatible elements in amphibole suggests a transitional magmatic affinity.

Acknowledgements

This work was supported by Fondecyt grant 1161818. Several samples were collected during the development of the Anillo Antártico projects ARTG-04 and ACT-105 in which Andrés Gómez, Fernando Poblete and Moyra Montes participated. We are grateful to Captain Hugo Cárdenas and the crew of the Marypaz II for their support during several field campaigns in the Patagonian fjords. Constructive comments by Michel Grégoire, an anonymous reviewer and Co-Editor-in-Chief Greg Shellnut helped to significantly improve the manuscript.

References

Acevedo, R.D., Linares, E., Ostera, H.A., Valín-Aloerdi, M.L. 2002. La Hornblendita Ushuaia (Tierra del Fuego): Geoquímica y Geocronología. Rev Asoc Geol Argentina 57(2):133–142.

Aldanmaz, E., Pearce, J. A., Thirlwall, M. F., & Mitchell, J. G. (2000). Petro- genetic evolution of Late Cenozoic post-collision volcanism in western Anatolia, Turkey. *Journal of Volcanology and Geothermal Research*, *102*, 67–95.

Allen, R.B. 1982. Geología de la Cordillera Sarmiento, Andes Patagónicos, entre los 51° 00′ y 52° 15′ Lat. S, Magallanes, Chile. Servicio Nacional de Geología y Minería, Boletín 38:1–46.

Altherr, R., Topuz, ., Siebel, ., en, C., Meyer, H.P., Sat r, M., Lahaye, ., 2008. Geochemical and Sr–Nd–Pb isotopic characteristics of Paleocene plagioleucitites from the eastern Pontides (NE Turkey). Lithos 105, 149–161.

Anderson A.T., 1980a. Significance of hornblende in calc-alkaline andesites and basalts. American Mineralogist 65:837-851.

Anderson J.L., 1996. Status of thermobarometry in granitic batholiths. Transactions of the Royal Society of Edinburgh 87:125-138.

Annen, C., Blundy., J., Sparks, R. 2006. The genesis of intermediate and silicic magmas in deep crystal hot zones. Journal of Petrology 47:505–539.

Bachmann, O., Dungan, M. A. 2002. Temperature-induced Al-zoning in hornblendes of the Fish Canyon magma, Colorado. American Mineralogist 87:1062–1076.

Barbeau, D.L., Olivero, E.B., Swanson-Hysell, N.L., Zahid, K.M., Murray, K.E., Gehrels, G.E. 2009. Detrital-zircon geochronology of the eastern Magallanes foreland basin: implications for Eocene kinematics of the northern Scotia Arc and Drake Passage. Earth Planet Sc Lett 284:489–503.

Blatter, D.L., Sisson, T.W., Hankins, W.B. 2017. Crystallization of oxidized, moderately hydrous arc basalt at mid-to lower-crustal pressures: implications for andesite genesis. Contrib Mineral Petrol 166:861–886.

Boari, E., Tommasini, S., Laurenzi, M.A., Conticelli, S., 2009. Transition from ultrapotassic kamafugitic to sub-alkaline magmas: Sr, Nd, and Pb isotope, trace element and $^{40}Ar–^{39}Ar$ age data from the Middle Latin Valley volcanic field, Roman Magmatic Province, Central Italy. Journal of Petrology 50, 1327–1357.

Bruhn, R.L., Stern, C.R., de Wit, M.J. 1978. Field and geochemical data bearing on the development of a Mesozoic volcano-tectonic rift zone and back-arc basin in southernmost South America. Earth Planet Sci Lett 41:32–46.

Calderón, M., Fildani, A., Hervé, F., Fanning, C.M., Weislogel, A., Cordani, U. 2007a. Late Jurassic bimodal magmatism in the northern seafloor remnant of the Rocas Verdes basin, Southern Patagonian Andes. Geol Soc London 164:1011–1022.

Calderón, M., Hervé, F., Massonne, H-J., Tassinari, C.G., Pankhurst, R.J., Godoy, E., Theye,

T. 2007b. Petrogenesis of the Puerto Eden Igneous and Metamorphic Complex, Magallanes, Chile: late Jurassic anatexis of meta-greywackes and granitoid magma genesis. Lithos 93:17–38.

Calderón, M., Fosdick, J.C., Warren, C., Massonne, H-J., Fanning, C.M., Fadel Cury, L., Schwanethal, J., Fonseca, P.E., Galaz, G., Gaytán, D., Hervé, F. 2012. The low-grade Canal de las Montañas Shear Zone and its role on the tectonic emplacement of the Sarmiento Ophiolitic Complex and Late Cretaceous Patagonian Andes orogeny, Chile. Tectonophysics 524–525:165–185.

Calderón, M., Prades, C.F., Hervé, F., Avendaño, V., Fanning, C.M., Massonne, H-J., Theye, T., Simonetti, A. 2013. Petrological vestiges of Late Jurassic-Early Cretaceous transition from rift to back-arc basin in southernmost Chile: new age and geochemical data from the Capitán Aracena, Carlos III and Tortuga Ophiolitic complexes. Geoch J 47:201–217.

Calderón, M., Hervé, F., Fuentes, F., Fosdick, J., Sepúlveda, F., Galaz, G. 2016. Tectonic evolution of Paleozoic and Mesozoic Andean Complexes and the Rocas Verdes Ophiolites in Southern Patagonia in Geodynamic Evolution of the Southernmost Andes: Connections with Scotia Arc, 7–37. Springer Earth System Sciences.

Cashman, K.V., Stephen, R., Sparks, J., Blundy, J.D. 2017. Vertically extensive and unstable magmatic systems: A unified view of igneous processes. Science 355. DOI: 10.1126/science.aag3055

Chazot, G., Menzies, M.A., Harte, B. 1996. Determination of coefficients between apatite, clinopyroxene, amphibole and melt in natural spinel lherzolites from Yemen: Implications for wet melting of the lithospheric mantle. Geochimica et Cosmochimica Acta. Vol 60, No 3, pp. 423-437.

Cooper, G.F., Davidson, J.P., Blundy, J.D. 2016. Plutonic xenoliths from Martinique, Lesser

Antilles: Evidence for open system processes and reactive melt flow in island arc crust. Contrib. Mineral. Petrol. 171:87.

Crisp, J. 1984. Rates of magma emplacement and volcanic output. Journal of Volcanology and Geothermal Research 20:177–211.

Cunningham, W.D. 1994. Uplifted ophiolitic rocks on Isla Gordon, southernmost Chile: Implications for the closure history of the Rocas Verdes marginal basin and the tectonic evolution of the Beagle Channel region. J. South. Am. Earth Sci, 7, 135-147.

Dalziel, I.W.D. 1990. Circum-Pacific orogenic processes: A view from the Andes and Antarctides. In: Geology of the Andes and Its Relation to Hydrocarbon and Mineral Resources. Circum-Pacific Council for Energy and Mineral Resources, Earth Science Series 11, 13-22.

Davidson, J., Turner, S., Plank, T. 2012. Dy/Dy*: Variations Arising from Mantle Sources and Petrogenetic Processes. Journal of Petrology 54:525–537.

Davison, J., Turner, S., Handley, H., Macpherson, C., Dosseto, A.. 2007. Amphibole –sponge" in arc crust?. Geology, vol. 35, no. 9, 787–790.

DeBari, S. 1997. Evolution of magmas in continental and oceanic arcs: The role of the lower crust. The Canadian Mineralogist 35:501–519.

DeBari, S. M., Coleman, R. G. 1989. Examination of the deep levels of an island arc: evidence from the Tonsina ultramafic–mafic assemblage, Tonsina, Alaska. Journal of Geophysical Research 94:4373–4391.

DePaolo, D. J. 1981. Trace-element and isotopic effects of combined wallrock assimilation and fractional crystallization. Earth and Planetary Science Letters 53:189–202.

Dessimoz, M., Müntener, O., Ulmer, P., 2011. A case of hornblende dominated fractionation of arc magmas: The Chelan Complex (North Cascades, Washington), Contributions to

Mineralogy and Petrology 157:541-558.

Dott, R.H., Winn, R.D., de Wit, M.J., Bruhn, R.L. 1977. Tectonic and sedimentary significance of Cretaceous Tekenika Beds of Tierra del Fuego. Nature 266:620–622.

Edmonds, M., Cashman, K.V., Holness, M., Jackson, M. 2019. Architecture and dynamics of magma reservoirs. Phil. Trans. R. Soc. A 377: 20180298. http://dx.doi.org/10.1098/rsta.2018.0298

Erdmann, S., Martel, C., Pichavant, M., Kushnir, A. 2014. Amphibole as an archivist of magmatic crystallization conditions: problems, potentia , and implications for inferring magma storage prior to the paroxysmal 2010 eruption of Mount Merapi, Indonesia. Contrib Mineral Petrol 167:1–23

Fildani, A., Cope, T.D., Graham, S.A., Wooden, J.L. 2003. Initiation of the Magallanes foreland basin: timing of the southernmost Patagonian Andes orogeny revised by detrital zircon provenance analysis. Geology 31:1081–1084.

Fosdick, J.C., Romans, B.W., Fildani, A., Bernhardt, A., Calderón, M., Graham, S.A. 2011. Kinematic evolution of the Patagonian retroarc fold-thrust belt and Magallanes foreland basin, Chile and Argentina, 51° 30′ S. Geol Soc Am Bull 123:1679–1698.

Ghiglione, M.C., Ramos, V.A. 2005. Chronology of deformation in the Southernmost Andes of Tierra del Fuego. Tectonophysics 405:25–46.

Gill, J. 1981. Orogenic Andesites and Plate Tectonics. Berlin: Springer, 390 pp.

Glazner, A. F. 1994. Foundering of mafic plutons and density stratification of continental crust. Geology 22:435–438.

Gómez, A. 2015. Petrología del Complejo de Gabros de las islas Caroline, Thomas, Sidney y

London, Batolito Fueguino: XII Región de Magallanes y de la Antártica chilena, Chile. Repositorio académico de la Universidad de Chile.

González Guillot, M. 2016. Magmatic evolution of the southernmost Andes and its relation with subduction processes. In: Ghiglione, M. (Ed.), Geodynamic Evolution of the Southernmost Andes: Connections with the Scotia Arc. Springer International Publishing, 37-74. ISBN: 978-3-319-39725-2.

onz lez uill ot, M., Escayola, M., Acevedo, R.D., Pimentel, M., Seraphim, ., Proenza, J., Schalamuk, I., 2009. The Plut n Dior tico Moat: Mildly alkaline monzonitic magmatism in the Fuegian Andes of Argentina. Journal of South American Earth Sciences, 28, 345-359.

onz lez uill ot, M., Escayola, M., Acevedo, R., 2011. Calc-alkaline rear-arc magmatism in the Fuegian Andes: implications for the mid-Cretaceous tectonomagmatic evolution of southernmost South America. Journal of South American Earth Sciences, 31, 1-16.

González Guillot, M., Ghiglione, M., Escayola, M., Martins Pimentel, M., Mortensen, J., Acevedo, R. 2018. Ushuaia pluton: Magma diversification, emplacement and relation with regional tectonics in the southernmost Andes. Journal of South American Earth Sciences 88. 10.1016/j.jsames.2018.10.001.

Grove, T. L. and Kinzler, R. J. 1986. Petrogenesis of andesites. Annual Review of Earth and Planetary Sciences 14: 417–454.

Hammarstrom J.M., Zen E-an., 1986. Aluminum in hornblende: An empirical igneous geobarometer. American Mineralogist 71:1297-1313.

Hanes, J.A., York, D., Hall, C.M., 1985. An 40Ar/39Ar geochronological and electron micro- probe investigation of an Archean pyroxenite and its bearing on ancient atmospheric compositions. Can. J. Earth Sci. 22:947–958. http://dx.doi.org/10.1139/e85-

100.

Hawkesworth, C.J., Gallagher, K., Hergt, J.M., Mcdermott, F., 1993. Mantle and slab contributions in arc magmas. Annual Review of Earth and Planetary Sciences 21, 175–204.

Hervé, F., Nelson, E., Kawashita, K., Suárez, M. 1981. New isotopic ages and the timing of orogenic events in the Cordillera Darwin, southernmost Chilean Andes. Earth and Planetary Science Letters 55:257–265.

Hervé, M., Suárez, M., Puig, A. 1984. The Patagonian Batholith S of Tierra del Fuego, Chile: timing and tectonic implications. Journal Geological Society of London 141:909–917.

Hervé, F., Pankhurst, R. J., Fanning, C. M., Calderón, M., Yaxley, G. M. 2007. The South Patagonian batholith: 150 my of granite magmatism on a plate margin. Lithos 97:373–394.

Hildreth, W., Moorbath, S. 1988. Crustal contribution to arc magmatism in the Andes of Central Chile. Contributions to Mineralogy and Petrology 98, 455–489.

Hilyard, M., Nielsen, R.L., Beard, J.S., Patino-Douce, A. and Blencoe, J. 2000. Experimental determination of the partitioning behavior of rare Earth and high field strength elements between pargasitic amphibole and natural silicate melts. Geochimica et Cosmochimica Acta 64: 1103-1120.

Hollister L.S., Grissom G.C., Peters E.K., Stowell H.H., Sisson V.B., 1987. Confirmation of the empirical correlation of Al in hornblende with pressure of solidification of calc-alkaline plutons. American Mineralogist 72:231-239.

Holness, M.B., Nielsen, T.F.N., Tegner, C. 2007. Textural maturity of cumulates: a record of chamber filling, cooling rate and large-scale convection in layered intrusions. Journal of Petrology 48:141–157.

Holloway, J.R., Burnham, C.W. 1972. Melting relations of basalt with equilibrium water pressure less than total pressure. Journal of Petrology 13:1-29.

Ireland, T.R., Clement, S., Compston, W., Foster, J.J., Holden, P., Jenkins, B., Lanc, P., Schram, N., Williams, I.S. 2008. Development of SHRIMP. Australian Journal of Earth Sciences, 55(6-7), 937-954.

Jackson, M.D., Blundy, J.D., Sparks, S. J. 2018. Chemical differentiation, cold storage and remobilization of magma in the Earth's crust. Nature 564.https://doi.org/10.1038/s41586-018-0746-2

Jagoutz, O., Kelemen, P.B. 2015. Role of Arc Processes in the Formation of Continental Crust. Annu. Rev. Earth Planet. Sci. 43:363–404.

Johnson M.C. and Rutherford M.J., 1989. Experimental calibration of the aluminum-in-hornblende geobarometer with application to Long Valley caldera (California) volcanic rocks. Geology 17: 837-841.

Katz, H.R., Watters, W.A., 1966. Geological investigation of the Yahgan Formation (Upper Mesozoic) and associated igneous rocks of Navarino Island, Southern Chile. N. Z. J. Geol. Geophys. 9:323–359. http://dx.doi.org/10.1080/00288306. 1966.10422818.

Kay, R. W. and Kay, S. M. 1993. Delamination and delamination magmatism. Tectonophysics 219:177–189.

Klepeis, K.A. 1994. The Magallanes and El Deseado fault zones: major segments of the South American – Scotia transform plate boundary in southernmost South America, Tierra del Fuego. J. Geophys. R. 99(B11): 22001 – 22014.

Klepeis, K.A., Lawyer, L.A. 1996. Tectonics of the Antartica – Scotia plate boundary near Elephant and Clarence Islands, West Antartica. J. Geophys. Res. 101: 20211 – 20231.

Klepeis, K., Betka, P., Clarke, G., Fanning, M., Hervé, F., Rojas, L., Mpodozis, C., Thomson, S. 2010. Continental underthrusting and obduction during the Cretaceous closure of the Rocas Verdes rift basin, Cordillera Darwin, Patagonian Andes. Tectonics 29.

Kohn, M.J., Spear, F.S., Harrison, T.M., Dalziel, I.W.D. 1995. $^{40}Ar/^{39}Ar$ geochronology and P-T-t paths from the Cordillera Darwin Metamorphic Complex, Tierra del Fuego, Chile. J Metam Geol 13:251–270.

König, M., Jokat, W. 2006. The Mesozoic breakup of the Weddell Sea. Journal of geophysical Research111: B12102.

Krawczynski, M.J., Grove, T.L., Behrens, H., 2012. Amphibole stability in primitive arc magmas: effects of temperature, H2O content, and oxygen fugacity, Contributions to Mineralogy and Petrology 164(no. 2): 1-27.

Larocque, J., Canil, D. 2010. The role of amphibole in the evolution of arc magmas and crust: the case from the Jurassic Bonanza arc section, Vancouver Island, Canada, Contributions to Mineralogy and Petrology 159: .475-492.

Leake, B., Wooley, A., Birch, W., et al. 1997. Nomenclature of amphiboles: report of the subcommittee on amphiboles of the international mineralogical association, commission on new minerals and mineral names. The Canadian Mineralogist: 35: 219- 246.

Lee, J-Y., Marti, K., Severinghaus, J.P., Kawamura, K., Yoo, H-S., Lee, J.B. and Kim, J.S. 2006. A redetermination of the isotopic abundances of atmospheric Ar. Geochimica et Cosmochimica Acta 70:4507-4512.

Lee, T.A., Bachmann, O. 2014. How important is the role of crystal fractionation in making intermediate magmas? Insights from Zr and P systematics. Earth Planet. Sci. Lett. 393:266–274.

Ludwig, K.R. 2001. User's Manual for Isoplot/Ex rev. 2.49. A Geochronological Toolkit for Microsoft Excel. Berkeley Geochronology Center Special Publication, Vol. 1a, 2001, pp. 1-55.

Ludwig, K.R. 2012. User's Manual for Isoplot 3.75 A e ochronological Toolkit for Microsoft Excel. Berkeley Geochronology Center Special Publication No. 5, 75 pp. Berkeley, California.

Macdonald, R., Hawkesworth, C. J., Heath E. 2000. The Lesser Antilles volcanic chain: a study in arc magmatism. Earth Sci. Rev. 49: 1–76.

Magee, C., Stevenson, C.T., Ebmeier, S.K., Keir, D., Hammond, J.O., Gottsmann, J., haler, K., Schofield, N., Jackson, C., Petronis, M., O'Driscoll, B., Morgan, J., Cruden, A., Vollgger, S., Dering, G., Micklethwaite, S., Jackson, M. 2018. Magma Plumbing Systems: A Geophysical Perspective Journal of Petrology, Volume 59, Issue 6, Pages 1217–1251, https://doi.org/10.1093/petrology/egy064

Maloney, K., Clarke, G., Klepeis, K., Fanning, C. Wang, W. 2011. Crustal growth during back-arc closure: Cretaceous exhumations history of Cordillera Darwin, southern Patagonia. Journal of metamorphic geology 29:649-672.

Massonne H.-J., Opitz J., Theye T. & Nasir S. 2013: Evolution of a very deeply subducted metasediment from As Sifah, northeastern coast of Oman. *Lithos* 156–159, 171–185.

Melekhova, E., Blundy, J., Robertson, R., Humphreys, M.C. 2011. Experimental evidence for polybaric differentiation of primitive arc basalt beneath St. Vincent, Lesser Antilles. J Petrol 56:161–192.

Melekhova, E., Blundy, J., Robertson, R., Humphreys, MC. 2015. Experimental evidence for polybaric differentiation of primitive arc basalt beneath St. Vincent, Lesser Antilles. J Petrol 56:161–192.

Miller, C.A., Barton, M., Hanson, R.E., Fleming, T.H., 1994. An Early Cretaceous volcanic arc/ marginal basin transition zone, Peninsula Hardy, southernmost Chile. J. Volcanol. Geotherm. Res. 63:33–58. http://dx.doi.org/10.1016/0377-0273(94)90017-5.

Morrison, G.W. 1980. Characteristics and tectonics of the shoshonite rock association. Lithos 13: 97–108.

Mukasa, S.B., Dalziel, I.W.D., 1996. Southernmost Andes and South Georgia Island, North Scotia Ridge: Zircon U–Pb and muscovite 40Ar/39Ar age constraints on tectonic evolution of Southwestern Gondwanaland. J. South Am. Earth Sci. 9: 349–365. http://dx. doi.org/10.1016/S0895-9811(96)00019-3.

M nker , C., r ner, ., o godzisnki, ., Churikova, T., 2004. Behavior of high field strength elements in subduction zones: constraints from Kamchatka-Aleutian arc lavas. Earth and Planetary Science Letters 224 (3–4), 275–293.

Müntener, O., Kelemen, P.B., Grove, T.L. 2000. The role of H2O during crystallization of primitive arc magmas under uppermost mantle conditions and genesis of igneous pyroxenites: an experimental study. Contributions to Mineralogy and Petrology vol. 141, 643-658.

Müntener, O., Kelemen, P. B., Grove, T. L. 2001. The role of H2O during crystallization of primitive arc magmas under upper- most mantle conditions and genesis of igneous pyroxenites: an experimental study. Contributions to Mineralogy and Petrology 141:643–658.

Müntener, O., Ulmer, P. 2006. Experimentally derived high-pressure cumulates from hydrous arc magmas and consequences for the seismic velocity structure of lower arc crust. Geophysical Research Letters 33: 21.

Nandedkar R.H., Ulmer P., Müntener O., 2014. Fractional crystallization of primitive,

hydrous arc magmas: an experimental study at 0.7 GPa. Contributions to Mineralogy and Petrology 167:1-27.

Nelson, E., Dalziel, I.W.D., Milnes, A.G. 1980. Structural geology of the Cordillera Darwin: collision style orogenesis in the southernmost Chilean Andes. Eclogae Geologicae Helveticae 73:727–751.

Pankhurst, R.J., Weaver, S.D., Hervé, F., Larrondo, P. 1999. Mesozoic–Cenozoic evolution of the North Patagonian Batholith in Aysén, southern Chile. Journal of the Geological Society of London, 156: 673-694.

Pankhurst, R. J., Riley, T. R., Fanning, C. M., Kelley, S. P. 2000. Episodic silicic volcanism in Patagonia and the Antarctic Peninsula: chronology of magmatism associated with the break– up of Gondwana. Journal of Petrology 41:605–625.

Parkinson I. J., Arculus R. J. 1999. The redox state of subduction zones: insights from arc peridotites. Chem. Geol. 160:409–423.

Pearce, J.A., Peate, D.W., 1995. Tectonic implications of the composition of volcanic arc magmas. Annual Review of Earth and Planetary Science 23, 251–285.

Pearce, J. A., van der Laan, S. R., Arculus, R. J., Murton, B. J., Ishii, T., Peate, D. W. Parkinson, I. J. 1992. Boninite and harzburgite from LEG125 (Bonin^Mariana Forearc): a case study of magma genesis during the initial stages of subduction. In: Fryer, P., Pearce, J. A. and Stokking, L. B. (eds) Proceedings of the Ocean Drilling Program, Scientific Results, 125. College Station, TX: Ocean Drilling Program:623-657.

Peressini, G., Quick, J. E., Sinigoi, S., Hofmann, A. W. & Fanning, M. 2007. Duration of a large mafic intrusion and heat transfer in the lower crust: a SHRIMP U-Pb zircon study in the Ivrea-Verbano zone (Western Alps, Italy). *J. Petrol.* 48:1185–1218.

Pichavant, M., Macdonald, R. 2007. Crystallization of primitive basaltic magmas at crustal

pressures and genesis of the calc-alkaline igneous suite: experimental evidence from St Vincent, Lesser Antilles arc. Contrib Mineral Petrol 154:535–558.

Pichavant, M., Martel, C., Bourdier, J.L., Scaillet B. 2002. Physical conditions, structure, and dynamics of a zoned magma chamber: Mount Pelée (Martinique, Lesser Antilles Arc). J Geophys Res 107:2093.

Poblete, F., Roperch, P. Arriagada, C., Ruffet, G., Ramírez de Arellano, C., Hervé, F., Poujol, M. 2015. Late Cretaceous – Early Eocene counterclockwise rotation of the Fuegian Andes and evolution of the Patagonia–Antartica Peninsula System. Tectonophysic. http://dx.doi.org/10.1016/j.tecto.2015.11.025

Prouteau, G., Scaillet, B. 2003. Experimental constraints on the origin of the 1991 Pinatubo dacite. Journal of Petrology 44, 2203–2241

Putirka, K., 2016. Amphibole thermometers and barometers for igneous systems and some implications for eruption mechanisms of felsic magmas at arc volcanoes. American Mineralogist 101:841-858.

Olivero, E.B., Malumián, N. 2008. Mesozoic-Cenozoic stratigraphy of the Fuegian Andes, Argentina. Geologica Acta 6:5–18

Raia, F., Spera, F. J. 1997. Simulation of the growth and differentiation of continental crust. Journal of Geophysical Research 102:22629–22648.

Renne, P.R., Blaco, G., Ludwig, K.R., Mundil, R. and Min, K. 2011. Response to the comment by .H. Schwarz et al. on "Joint determination of 40K decay constants and 40Ar*/40K for the Fish Canyon sanidine standard, and improved accuracy for 40Ar/39Ar geochronology" by P.R. Renne et al. (2010). Geochimica et Cosmochimica Acta 75:5097-5100.

Ridolfi, F., Renzulli, A. 2012. Calcic amphiboles in calc- alkaline and alkaline magmas:

thermobarometric and chemometric empirical equations valid up to 1,130°C and 2.2 GPa. Contributions to Mineralogy and Petrology 163:877-895.

Ridolfi F., Renzulli A., Puerini M. 2010. Stability and chemical equilibrium of amphibole in calc-alkaline magmas: an overview, new thermobarometric formulations and application to subduction-related volcanoes. Contributions to Mineralogy and Petrology 160, 45-66.

Roddick, J.C., Cliff, R.A., Rex, D.C., 1980. The evolution of excess argon in alpine biotites—a 40Ar–39Ar analysis. Earth Planet. Sci. Lett. 48:185–208.

Roggensack, K., Hervig, R. L., McKnight, S. B., Williams, S. N. 1997. Explosive basaltic volcanism from Cerro Negro volcano: influence of volatiles on eruptive style. Science 277:1639–1642.

Romans, B.W., Fildani, A., Graham, S.A., Hubbard, S.M., Covault, J.A. 2010. Importance of predecessor basin history on sedimentary fill of a retroarc foreland basin: provenance analysis of the Cretaceous Magallanes basin, Chile (50°52′S). Basin Research 22:640–658.

Rudnick, R. L., Fountain, D. M. 1995. Nature and composition of the continental crust: a lower crustal perspective. Reviews of Geophysics 33:267–309.

Ruffet, G., Feraud, G., Amouric, M., 1991. Comparison of ^{40}Ar–^{39}Ar conventional and laser dating of biotites from the North Trégor Batholith. Geochim. Cosmochim. 55:1675–1688.

Ruffet, G., Féraud, G., Balèvre, M., Kiénast, J.-R., 1995. Plateau ages and excess argon in phengites: an ^{40}Ar–^{39}Ar laser probe study of Alpine micas (Sesia Zone, Western Alps, northern Italy). Chem. Geol. 121:327–343. http://dx.doi.org/10.1016/0009-2541(94)00132-R.

Schmidt M.W., 1992. Amphibole composition in tonalite as a function of pressure: an experimental calibration of the Al- in-hornblende barometer. Contributions to Mineralogy and Petrology 110:304-310.

Sellés, D. 2006. Stratigraphy, petrology, and geochemistry of Nevado de Longaví volcano: Chilean Andes (36.2°S). Thèse de doctorat : Univ. Genève, no. Sc. 3752.

Seton, M., M l ler, R.D., ahirovic, S., a ina, C., Torsvik, T., Shephard, ., Talsma, A., Gurnis, M., Turner, M., Maus, S., Chandler, M., 2012. Global continental and ocean basin re- constructions since 200 Ma. Earth Sci. Rev. 113, 212–270. http://dx.doi.org/10.1016/j.earscirev.2012.03.002.

Sisson T.W., Grove T.L. 1993. Experimental investigations of the role of H2O in calc-alkaline differentiation and subduction zone magmatism. Contributions to Mineralogy and Petrology 113:143-166.

Smith, D.J. 2014. Clinopyroxene precursors to amphibole sponge in the arc crust. Nat. Commun. 5:4329. doi: 10.1038/ncomms5329.

Sobolev, A. V., Chaussidon, M. 1996. H_2O concentrations in primary melts from supra-subduction zones and mid-ocean ridges. Earth Planet. Sci. Lett. 137:45–55.

Solano, J.M.S, Jackson, M.D., Sparks, R.S.J., Blundy, J.D., Annen, C. 2012. Melt segregation in deep crustal hot zones: a mechanism for chemical differentiation, crustal assimilation and the formation of evolved magmas. Journal of Petrology, Vol. 53, 1999-2026.

Stern, C.R., de Wit, M.J. 2003. Rocas Verdes ophiolites, southernmost South America: remnants of progressive stages of development on oceanic-type crust in a continental margin back-arc basin. In: Dilek Y, Robinson PT (eds) Ophiolites in earth history 218:1–19.

Stern, C. R., Killian, R. 1996. Role of the subducted slab, mantle wedge and continental crust in the generation of adakites from the Andean Austral Volcanic Zone. Contrib Mineral Petrol 123:263 – 281.

Suárez, M. 1977. Notas geoquimicas preliminares del Batolito Patagonico al sur de Tierra del Fuego, Chile. Rev.geol. Chile 4:15-33.

Suárez, M., Hervé, M., Puig, A. 1985. Hoja Isla Hoste e Islas Adyacentes, XII Región. Carta geológica de Chile, Servicio Nacional de Geología y Minería, número 65.

Su rez, M., Herv , M., Puig, A., 1986. K–Ar dates on granitoids from Archipelago Cabo de Hornos, southernmost Chile. Geological Magazine 123, 581-584.

Tiepolo, M., Tribuzio, R. 2008. Petrology and U-Pb zircon geochronology of amphibole-rich cumulates with sanukitic affinity from Husky Ridge (Northern Victoria Land, Antarctica): insights into the role of amphibole in the petrogenesis of subduction-related magmas. Journal of Petrology 49:937-970.

Tiepolo, M., Tribuzio, R., Langone, A. 2011. High-Mg Andesite Petrogenesis by Amphibole Crystallization and Ultramafic Crust Assimilation: Evidence from Adamello Hornblendites (Central Alps, Italy). Journal of Petrology 52, 1011-1045.

Torres Carbonell, P.J. Cao, S.J. & Dimieri, L.V. 2017. Spatial and temporal characterization of progressive deformation during orogenic growth: Example from the Fuegian Andes, southern Argentina. Journal of Structural Geology, 99, 1-19. http://doi.org/https://doi.org/10.1016/j.jsg.2017.04.003

Turner, G., 1971. ^{40}Ar–^{39}Ar ages from the lunar Maria. Earth Planet. Sci. Lett. 11:169–191.

Turner, S.P., 2005. Some remarks on magmatic processes beneath island arc volcanoes. Advances in Science, Earth Sciences. Imperial College Press, pp. 131–155.

Voshage, H., Hofmann, A. W., Mazzucchelli, M., Rivalenti, G., Sinigoi, S., Raczek, I., Demarchi, G. 1990. Isotopic evidence from the Ivrea Zone for a hybrid lower crust formed by magmatic underplating. *Nature* 347:731–736.

Yavuz F., Döner, Z. 2017. WinAmptb: A Windows program for calcic amphibole thermobarometry. Period. Mineral. 86:135-167.

Figure Captions.

Figure 1. Geological sketch map of the southernmost Andes of South America (modified from Suárez et al., 1985 and Sernageomin, 2003). Paleozoic and Mesozoic lithostratigraphic units are illustrated, including the Rocas Verdes ophiolites, folded and sheared volcanic and sedimentary successions of the Tobífera, Hardy, Zapata, Yahgán formations, the Patagonian and Fuegian batholiths, and metamorphic complexes. **b.** Inset shows the location of samples from the Fuegian Batholith and other geological units in Tierra del Fuego as well as main geological units. Abbreviations are: BC, Beagle Channel; CD, Cordillera Darwin; IL, Isla Londonderry; IT, Isla Thomas; IN, Isla Navarino; U, Ushuaia.

Figure 2. Representative mineral assemblages of samples. **a.** Overview of medium-grained hornblendite (FB) with idiomorphic hornblende and exsolved Fe-Ti oxides and interstitial plagioclase. **b.** Pegmatitic hornblendite dyke with coarse amphibole and interstitial plagioclase that occurs as fine-grained aggregates. **c.** Tonalite with plagioclase, quartz, amphibole, biotite and titanite. All phases are homogenous and lack compositional zoning. **d.** Gabbro assemblage with plagioclase and minor amphibole with relict inclusions of clinopyroxene, interstitial biotite and Fe-Ti oxides. **e.** Medium-grained gabbro with homogenous plagioclase, clinopyroxene and amphibole weakly replaced by chlorite. **f.** Lamprophyre dyke with microporphyritic texture and phenocrysts of amphibole and clinopyroxene in a groundmass of plagioclase, amphibole and chlorite pseudomorphs. **g.** hornblendite (UP) with amphibole, plagioclase and magmatic epidote. In some amphibole crystals, rare relicts of presumed clinopyroxene are observed. **h.** Main assemblage of hornblende-monzodiorite, amphibole, plagioclase, large titanite crystals with minor interstitial k-feldspar.

Figure 3. SHRIMP U-Pb isotopic data from zircon. **a**, **b** and **c**, show Tera–Wasserberg concordia plots, calculated mean ages (with errors reported at 2σ level) for analysed zircon samples FC1854 (hornblende tonalite), AA1419 (segregation tonalite) FC1811 and (clinopyroxene-hornblende gabbro), respectively.

Figure 4. Whole-rock chondrite-normalized REE patterns (Sun and McDonough, 1989) in comparison with amphibole patterns (shaded gray). **a**. Hornblendites (FB). **b,c,d** Gabbro–tonalite samples. **e.** Monzodiorite (UP). **f.** Lamprophyre.

Figure 5. Comparison of εNd_i vs $(^{87}Sr/^{86}Sr)_I$ from the South Patagonian Batholith (Hervé et al., 2007), hornblendites and tonalite from the Fuegian Batholith (hb: hornblendite; hb-p: hornblendite pegmatitic; ton: tonalite).

Figure 6. EMPA composition of amphibole in selected samples. Classification after Leake et al. (1997). FB: Fuegian Batholith. UP: Ushuaia Pluton.

Figure 7. Chondrite-normalized REE and incompatible element patterns for amphibole. Normalization values are from Sun and McDonough (1989).

Figure 8. EMPA and LA-ICP-MS composition of amphibole. **a.** Si (a.p.f.u) vs. Na + K in Ca-amphibole. The dash line separates the Mg-hastingsite and pargasite domain (early amphibole) from the Mg-hornblende to tsch-horblende domains (late amphibole). **b.** Al^{VI} vs Mg# in Ca-

amphibole. **c.** Eu/Eu* vs La/Sm in Ca-amphibole. **d.** Eu/Eu* vs Mg#. **e.** Dy/Dy* vs Dy/Yb after Davidson et al. (2012).

Figure 9. Sketches illustrating the evolution of the Fuegian Batholith and Fuegian orogen in the tectonic framework of the Rocas Verdes Basin.

Table titles

Table 1. Summary of the different plutonic complexes and main features of the Fuegian Batholith (Suárez et al., 1977, 1979; Hervé et al., 1984) and the Ushuaia Pluton (Acevedo et al., 2002; González-Guillot et al., 2009, 2018).

Fuegian Batholith	**Age**	**Lithology**	**Features**
Gabbro Complex	141 - 103 Ma (K-Ar whole rock)	Gabbros and hornblendites	Common cumulate textures with no penetrative foliation.
Canal Beagle Plutonic Complex	113 - 81 Ma (K-Ar whole rock; Rb-Sr isochron)	Tonalite and granodiorite with subordinate quartz-monzodiorites and quartz-diorites	Penetrative foliation of synmagmatic origin
Seno Año Nuevo Plutonic Complex	60 - 34 Ma (K-Ar whole rock; Rb-Sr isochron)	Quartz-diorites to granites, with tonalite and quartz monzodiorites as the most common.	Slight K enrichment with no penetrative magmatic foliation
Ushuaia	**Age**	**Lithology**	**Features**
Ushuaia Pluton	113 ± 5 Ma (K-Ar whole rock) 101.9 ± 2.8 Ma (K-Ar amph) 75±1 Ma (U-Pb in gabbro pocket)	hornblende pyroxenite, hornblendites, gabbros and monzodiorite and quartz-monzodiorite	Two lithologically distinc sections; ultramafic and intermediate with K enrichment

Moat Pluton	115 ± 3 Ma (Rb-Sr isochron)	Diorite, gabbros, monzodiorites, monzogabbros and monzonites with isolated hornblendite and pyroxenite.	Ultramafic rocks are common as autoliths arranged parallel to the magmatic foliation or layered in isolated outcrops

Table 2. SHRIMP U-Pb zircon results on samples hornblende tonalite (FC1854), segregation of tonalite (AA1419) and clinopyroxene-hornblende gabbro (FC1811).

Table 2a. Summary of SHRIMP U-Pb results for zircons from hornblende tonalite sample FC1854.

Grain spot	U (ppm)	Th (ppm)	Th/U	$^{206}Pb^*$ (ppm)	$^{204}Pb/^{206}Pb$	$f_{206\%}$	$^{238}U/^{206}Pb$	±	$^{207}Pb/^{206}Pb$	±		$^{206}Pb/^{238}U$	±		$^{206}Pb/^{238}U$	±
1.1	123.9347002	45.01692991	0.363231039	2.0	-	<0.01	52.88668398	0.80893038 5	0.0478	0.0021		0.0189	0.0003		120.8	1.9
2.1	197.0640407	87.54046632	0.44422341	3.3	-	0.09189822 1	50.75731224	0.90315484	0.0493	0.0015		0.0197	0.0004		125.7	2.2
3.1	355.6766755	193.1005103	0.54291024 3	6.1	0.000436	0.36777407 6	50.45828805	0.62963582 1	0.0515	0.0013		0.0197	0.0002		126.0	1.6
4.1	476.6770699	367.1730329	0.77027626 5	7.9	0.000590	0.11083744 7	51.91940797	0.72524010 7	0.0494	0.0010		0.0192	0.0003		122.8	1.7
5.1	250.4844897	132.577016	0.52928233 7	4.2	-	0.15660110 8	51.43025246	0.66106836 8	0.0497	0.0014		0.0194	0.0003		123.9	1.6
6.1	313.1142016	169.1188224	0.54011865 8	5.2	0.000453	<0.01	52.08782713	0.63215508	0.0479	0.0012		0.0192	0.0002		122.7	1.5

7.1	274.2346089	118.7939158	0.43318352 9	4.8	0.000850	<0.01	49.3691685 8	0.66236733 8	0.0482	0.0014		0.0203	0.0003		129.3	1.7
8.1	112.8363719	65.48643523	0.58036636 7	1.9	0.000501	0.11018984 6	51.9911401 3	0.82145707 8	0.0494	0.0022		0.0192	0.0003		122.7	2.0
9.1	154.6780661	58.48052745	0.37807899 3	2.6	0.001094	0.17275738 3	51.3864315 2	0.73155298 4	0.0499	0.0018		0.0194	0.0003		124.0	1.8
10.1	288.2221648	240.9918522	0.83613226 8	4.8	0.000227	0.09627679 5	51.5670284 7	0.63305638 5	0.0493	0.0012		0.0194	0.0002		123.7	1.5
11.1	298.9658883	209.5511174	0.70091982 3	4.9	-	<0.01	52.8536860 8	0.65673873 4	0.0484	0.0013		0.0189	0.0002		120.8	1.5
12.1	178.0339454	135.9925297	0.76385730 5	3.0	-	<0.01	50.7507872 9	0.77163376 4	0.0477	0.0017		0.0197	0.0003		125.9	1.7
13.1	130.499231	53.01462182	0.40624470 7	2.1	0.000302	0.69595577	52.2367224 4	0.77321188 7	0.0540	0.0020		0.0190	0.0003		121.4	1.8
14.1	171.8649627	101.2346375	0.58903592 6	2.8	-	<0.01	52.9831200 4	0.74404379	0.0469	0.0017		0.0189	0.0003		120.8	1.7
15.1	157.2969709	60.19152527	0.38266169 4	2.8	-	<0.01	53.3167405	0.75465526 7	0.0471	0.0018		0.0188	0.0003		120.0	1.7
15.2	311.4712385	265.295783	0.85178505	5.1	0.001652	0.02702155 6	52.6059380 3	0.65703463	0.0487	0.0013		0.0190	0.0002		121.4	1.5
16.1	226.8307054	112.9452237	0.49792740 2	3.7	0.000982	<0.01	52.8057604 6	0.68907264 4	0.0483	0.0016		0.0189	0.0003		121.0	1.6
17.1	230.0103503	185.2677678	0.80547578 6	3.7	0.000022	0.07285403 9	53.2592536 9	0.68327414 6	0.0490	0.0019		0.0188	0.0002		119.8	1.6
18.1	121.4764162	40.55098993	0.33381779 9	2.0	0.001867	<0.01	53.2638325 9	0.81004997 4	0.0477	0.0020		0.0188	0.0003		120.0	1.8
19.1	204.730568	74.5257872	0.36401885	3.3	0.000270	<0.01	52.9158340	0.70612724	0.0483	0.0015		0.0189	0.0003		120.7	1.6

	5	2	5				1								
20.1	105.720618	39.9667705 8	0.37804140 1	1.7	0.001591	0.59140449 1	52.5733362 4	0.83467677 7	0.0531	0.0023		0.0189	0.0003		120.8	1.9
20.2	187.2688858	82.4029878 3	0.44002498	3.1	0.000677	0.00102563 9	52.4912616 1	0.71302776 5	0.0485	0.0016		0.0191	0.0003		121.7	1.7
21.1	323.6302232	154.6157448	0.47775434 4	5.3	0.000505	0.08426458 6	52.3618483 8	0.63986371 4	0.0491	0.0015		0.0191	0.0002		121.9	1.5
22.1	139.6026597	51.1328970 7	0.36627451 9	2.3	0.002202	0.02728033 2	51.8103501 2	0.94081970 7	0.0487	0.0018		0.0193	0.0004		123.2	2.2
23.1	239.2187993	118.5762709	0.49568123 9	4.0	0.000004	0.06453157 9	50.8301955 4	0.80928876 2	0.0490	0.0014		0.0197	0.0003		125.5	2.0
24.1	125.7317447	46.1246100 3	0.36684936	1.9	0.003261	0.05585339 2	57.3011650 9	0.59212995 4	0.0487	0.0028		0.0174	0.0003		111.5	2.0
25.1	367.4833861	202.6246998	0.55138465 4	6.0	0.000125	0.01	52.9030798 8	0.63018490 3	0.0478	0.0011		0.0189	0.0002		120.8	1.4
26.1	178.4027296	104.0101367	0.58300754 1	2.9	0.000113	<0.01	52.1184491 5	0.71379145 6	0.0483	0.0016		0.0192	0.0003		122.5	1.7
27.1	59.80510324	18.3969687 4	0.30761536 6	1.0	0.001905	0.16282472 7	52.8403471 2	1.02477452 6	0.0497	0.0037		0.0189	0.0004		120.7	2.4
28.1	217.3744275	134.2552082	0.61762109 6	3.6	0.000050	<0.01	51.5662628 4	0.67385927	0.0474	0.0027		0.0194	0.0003		124.0	1.7

Calculated U-Pb zircon age: 122.3 ± 0.8

Notes: 1. Uncertainties given at the one σ level.
2. Error in Temora reference zircon calibration was 0.34% for the analytical session.
(not included in above errors but required when comparing data from different mounts).
3. f_{206} % denotes the percentage of ^{206}Pb that is common Pb.
4. Correction for common Pb for the U/Pb data has been made using the measured $^{238}U/^{206}Pb$ and $^{207}Pb/^{206}Pb$ ratios following Tera and Wasserburg (1972) as outlined in Williams (1998).

Table 2b. Summary of SHRIMP U-Pb results for zircons from tonalite segregation sample AA1419.

								Total				Radiogenic			Age (Ma)	
Grain spot	U (ppm)	Th (ppm)	Th/U	$^{206}Pb^*$ (ppm)	$^{204}Pb/^{206}Pb$	$f_{206\%}$	$^{238}U/^{206}Pb$	±	$^{207}Pb/^{206}Pb$	±		$^{206}Pb/^{238}U$	±		$^{206}Pb/^{238}U$	±
1.1	5221.945538	3762.224966	0.720464229	88.2	-	<0.01	50.87000414	0.52021583	0.0484	0.00003		0.0197	0.00002		125.5	1.3
2.1	366.3370714	135.2126945	0.369093671	6.0	0.000093	0.17061176	52.02951854	0.64106667	0.0498	0.00011		0.0192	0.00002		122.5	1.5
3.1	251.7325828	119.1994955	0.473516357	4.1	0.000216	0.41965244 3	52.74199948	0.70[illegible]5864	0.0518	0.00014		0.0189	0.00003		120.6	1.6
4.1	1848.787867	1567.37537	0.847785405	29.2	-	0.09823923[illegible]	54.[illegible]193[illegible]	0.59795448	0.0491	0.00005		0.0183	0.00002		117.0	1.3
5.1	433.8449541	335.7519293	0.773898431	7.2	0.000533	0.14380665[illegible]	51.82482401 78	0.62131710 6	0.0496	0.00010		0.0192	0.00002		122.9	1.5
6.1	642.3561813	256.3642555	0.399099 85	10.4	0.000023	0.05283042 6	52.96287303	0.60247592 7	0.0489	0.00008		0.0189	0.00002		120.5	1.4
7.1	1121.779359	554.3680588	0.494186[illegible]1	18.2	0.000001	0.15177707 3	53.08281043	0.59360232 2	0.0496	0.00006		0.0188	0.00002		120.1	1.3
8.1	3295.890514	2211.201625	0.67089656 5	55.4	0.000032	0.02375415	51.10703038	0.52507522 6	0.0487	0.00004		0.0196	0.00002		124.9	1.3
9.1	1287.440744	621.6418926	0.482850877	21.0	0.000083	0.04877672 9	52.67219047	0.56364114 9	0.0488	0.00006		0.0190	0.00002		121.2	1.3
10.1	367.160349	214.80158	0.585034796	6.0	-	0.23030698 6	52.26849532	0.63841183 1	0.0503	0.00017		0.0191	0.00002		121.9	1.5
11.1	237.0778387	89.80349146	0.378793277	4.0	-	0.20576450 4	51.22191741	0.67459697 3	0.0501	0.00014		0.0195	0.00003		124.4	1.6

12.1	1033.801836	466.7605353	0.45149903	17.4	0.000075	0.0105139933	51.1811148 1	0.55393834	0.0486	0.00 06		0.0195	0.00 02		124.7	1.3
13.1	250.1774661	122.7722847	0.49074078	4.1	-	0.13135406 2	52.0789263 8	0.67971620 5	0.0495	0.00 13		0.0192	0.00 03		122.4	1.6
14.1	1500.226834	872.9350738	0.58186872 4	24.5	-	0.05036351 7	52.5257111 6	0.55535042 8	0.0489	0.00 05		0.0190	0.00 02		121.5	1.3
14.2	222.6711771	87.35225463	0.39229259 8	3.7	-	0.01604163 3	51.1838152 5	0.67606584	0.0486	0.00 14		0.0195	0.00 03		124.7	1.7
15.1	630.1935629	387.3750758	0.61469221 3	10.4	-	0.12307751 3	51.8845398 3	0.58440834 5	0.0495	0.00 08		0.0192	0.00 02		122.9	1.4
16.1	1729.827005	1412.655092	0.81664529 9	29.1	0.000051	0.07207571 5	51.0262072 2	0.53487162 9	0.0491	0.00 05		0.0196	0.00 02		125.0	1.3
17.1	2275.775874	1990.842814	0.87479739 9	37.6	0.000008	0.07435240 3	52.0609198 9	0.53982678 5	0.0491	0.00 04		0.0192	0.00 02		122.6	1.3
17.2	153.5950477	59.37208867	0.38654949 8	2.5	-	0.20502501 4	52.1616962	0.75177135 2	0.0501	0.00 17		0.0191	0.00 03		122.2	1.8
18.1	1401.094984	1156.444991	0.82538657 6	23.1	0.000024	<0.01	51.3552325 7	0.54355238 8	0.0475	0.00 05		0.0195	0.00 02		124.5	1.3
19.1	956.9147942	523.7797095	0.54 7332 5	16.4	-	<0.01	50.1308771 3	0.54265932 1	0.0483	0.00 06		0.0200	0.00 02		127.4	1.4
20.1	1192.381371	820.762231	0.68833869	19.2	-	0.07467997 2	53.4329773 8	0.59082373 2	0.0490	0.00 06		0.0187	0.00 02		119.4	1.3
20.2	181.3414325	66.57275786	0.36711278 2	3.0	-	0.43610115 8	51.1424545 1	0.69989667 2	0.0520	0.00 15		0.0195	0.00 03		124.3	1.7
21.1	261.8685576	91.91119263	0.35098216 2	4.3	0.000519	0.23880435 9	52.5083262 9	0.67071205 3	0.0503	0.00 13		0.0190	0.00 02		121.3	1.6
22.1	535.978238	288.776606	0.53878 42	8.7	0.000236	0.24563214	52.6247864	0.60266419	0.0504	0.00 09		0.0190	0.00 02		121.1	1.4

	5	6				8	9	5							
23.1	1491.339465	1191.337193	0.79883703	24.2	0.000135	<0.01	52.9740150 8	0.56623553 3	0.0480	0.0005		0.0189	0.0002		120.6	1.3
24.1	2080.504598	1837.734138	0.88331174	34.8	-	<0.01	51.4140416 5	0.53404055 3	0.0483	0.0004		0.0195	0.0002		124.2	1.3
24.2	306.1511848	135.4483232	0.44242299 2	5.0	0.000023	0.26801638 5	52.369058	0.64628190 1	0.0506	0.0012		0.0190	0.0002		121.6	1.5
25.1	227.1853001	74.01092645	0.32577339 5	3.8	0.000535	0.34851905 3	50.9069396 3	0.66202357	0.0513	0.0013		0.0196	0.0003		125.0	1.6
26.1	1566.805479	2016.320638	1.28689914 9	26.2	0.000014	0.03953512 8	51.2892218 4	0.53781203	0.0488	0.0005		0.0195	0.0002		124.4	1.3

Calculated U-Pb zircon age : 122.9 ± 0.7

Notes: 1. Uncertainties given at the one σ level.
2. Error in Temora reference zircon calibration was 0.39% for the analytical session.
(not included in above errors but required when comparing data from different mounts).
3. f_{206} % denotes the percentage of ^{206}Pb that is common Pb.
4. Correction for common Pb for the U/Pb data has been made using the measured $^{238}U/^{206}Pb$ and $^{207}Pb/^{206}Pb$ ratios following Tera and Wasserburg (1972) as outlined in Williams (1998)

Table 2c. Summary of SHRIMP U-Pb results for zircons from clinopyroxene-hornblende gabbro sample FC1811.

Grain spot	U (ppm)	Th (ppm)	Th/U	$^{206}Pb^*$ (ppm)	$^{204}Pb/^{206}Pb$	$f_{206\%}$	$^{238}U/^{206}Pb$	±	$^{207}Pb/^{206}Pb$	±		$^{206}Pb/^{238}U$	±		$^{206}Pb/^{238}U$	±
1.2	105	52	0.49	0.8	-	<0.01	106.85	2.42	0.0444	0.0039		0.00939	0.00022		60.3	1.4
2.2	132	72	0.55	1.1	0.002141	<0.01	99.73	2.18	0.0461	0.0032		0.00974	0.00022		62.5	1.4
3.2	170	97	0.57	1.3	0.001757	<0.01	112.40	2.10	0.0464	0.0029		0.00912	0.00019		58.5	1.2
4.1	101	56	0.56	0.9	0.001447	0.17	100.61	2.23	0.0486	0.0039		0.00992	0.00023		63.6	1.4
5.1	584	718	1.23	4.8	0.000805	0.15	104.12	1.76	0.0484	0.0016		0.00959	0.00016		61.5	1.0

6.1	616	514	0.83	5.0	0.000458	<0.01	106.74	1.44	0.0467	0.0017		0.00937	0.00013		60.1	0.8
7.1	199	108	0.54	1.6	0.001243	0.73	107.39	1.93	0.0529	0.0029		0.00924	0.00017		59.3	1.1
8.1	293	244	0.83	2.4	0.001202	0.39	107.03	1.72	0.0503	0.0023		0.00931	0.00015		59.7	1.0
9.1	62	29	0.47	0.5	0.002196	0.52	108.30	3.11	0.0513	0.0052		0.00919	0.00027		58.9	1.7
10.1	94	49	0.52	0.8	0.004209	<0.01	104.52	2.45	0.0461	0.0031		0.00958	0.00023		61.5	1.5
11.1	170	80	0.47	1.4	0.001610	0.39	107.20	2.05	0.0503	0.0044		0.00929	0.00019		59.6	1.2
12.1	77	39	0.51	0.6	0.002369	1.16	107.12	2.75	0.0501	0.0048		0.00923	0.00024		59.2	1.6
13.1	75	40	0.54	0.6	0.003577	0.30	102.34	2.00	0.0496	0.0044		0.00974	0.00025		62.5	1.6
13.2	139	114	0.82	1.2	0.001503	0.57	108.50	3.76	0.0519	0.0033		0.00981	0.00021		62.9	1.4
14.1	273	186	0.68	2.3	0.000215	<0.01	102.84	1.68	0.0458	0.0024		0.00974	0.00016		62.5	1.0
15.1	112	62	0.55	0.9	0.000415	0.35	103.30	2.28	0.0500	0.0039		0.00965	0.00022		61.9	1.4
16.1	166	95	0.57	1.3	0.004653	0.43	107.73	2.04	0.0506	0.0030		0.00924	0.00018		59.3	1.1
17.1	58	30	0.51	0.5	0.002424	0.55	109.35	3.19	0.0515	0.0052		0.00909	0.00027		58.4	1.7
18.1	91	54	0.59	0.7	0.000941	<0.01	104.61	2.54	0.0461	0.0043		0.00957	0.00024		61.4	1.5
19.1	162	78	0.48	1.3	0.002357	0.52	103.94	2.01	0.0513	0.0035		0.00957	0.00019		61.4	1.2
19.2	48	22	0.45	0.4	0.006110	0.42	105.35	3.27	0.0505	0.0056		0.00945	0.00030		60.6	1.9
20.1	75	33	0.44	0.6	0.001953	0.64	107.67	2.83	0.0523	0.0048		0.00923	0.00025		59.2	1.6
21.1	336	377	1.12	2.7	0.001193	<0.01	104.87	1.57	0.0452	0.0020		0.00956	0.00015		61.3	0.9
22.1	173	110	0.	1.4	0.00	1.	107.	2.	0.05	0.0		0.00	0.0		58.9	1

			64		1137	05	79	07	55	033		918	0018			.2
23.1	153	83	0.54	1.2	0.001757	0.68	106.56	2.02	0.0526	0.0031		0.00932	0.00018		59.8	1.2
24.1	381	466	1.22	3.1	0.000151	<0.01	106.01	1.54	0.0445	0.0019		0.00947	0.00014		60.7	0.9
25.1	106	54	0.51	0.8	0.002489	0.14	113.57	2.64	0.0482	0.0039		0.00887	0.00023		56.9	1.5
26.1	122	62	0.51	1.0	0.001767	0.29	107.71	2.36	0.0495	0.0036		0.00926	0.00021		59.4	1.3
26.2	74	39	0.53	0.6	0.002037	1.84	106.60	3.99	0.0618	[illegible]52		0.00921	0.00035		59.1	2.2

Calculated U-Pb zircon age : 60.5 ± 0.6

Notes: 1. Uncertainties given at the one σ level.
2. Error in Temora reference zircon calibration was 0.50% for the analytical session.
(not included in above errors but required when comparing data from different mounts).
3. f_{206} % denotes the percentage of ^{206}Pb that is common Pb.
4. Correction for common Pb for the U/Pb data has been made using the measured $^{238}U/^{206}Pb$ and $^{207}Pb/^{206}Pb$ ratios following Tera and Wasserburg (1972) as outlined in Williams (1998).

Table 3. Bulk rock major element (wt.%), trace and rare earth elements (ppm) of the Fuegian Batholith, lamprophyre and hornblendite and monzodiorite from the Ushuaia Pluton.

Sample No	**130A P0I-030**	**130A P0I-031**	**130A P0I-041**	**FC1 854**	**FC1 811**	**AA1 418**	**TN0 713C**	**FO 218B**	**ST03 36B**	**FC08 35**	**MT2 89**	**MTF 1**	**MT7 0**
Locality	Fuegian Batholith	Fuegian Batholith	Fuegian Batholith	Fuegian Batholith	Fuegian Batholith	Fuegian Batholith	Tortuga Complex	SPB	Sarmiento Complex	Sarmiento Complex	Ushuaia Pluton	Ushuaia Pluton	Ushuaia Pluton
Lithology	Hornblendite	Hornblendite	Tonalite	Tonalite	Gabbro	Gabbro	Lamprophyre	Lamprophyre	Lamprophyre	Lamprophyre	Hornblendite	Hornblendite	Monzodiorite
Age	102.0 *			122.3 **	60.5 **	112.9 **	98.7 *						
SiO_2	38.90	43.18	70.93	57.49	47.01	45.5	48.05	44.47	40.61	45.21	39.99	43.00	55.62
TiO_2	1.43	1.33	0.48	0.75	0.99	0.4	0.96	1.34	1.15	1.05	1.61	1.51	0.72
Al_2O_3	21.21	19.43	13.91	17.88	19.52	28.18	16.35	14.18	11.68	13.22	15.47	12.19	17.05
FeOT	13.22	8.60	4.35	7.5	11.45	5.46	3.50	8.79	9.59	8.31	13.97	13.82	7.17

MnO	0.12	0.13	0.09	0.18	0.18	0.07	0.17	0.16	0.22	0.28	0.21	0.17	0.19
MgO	8.89	10.8	1.18	3.68	5.06	2.63	11.92	8.26	12.27	8.12	12.66	12.32	3.26
CaO	12.87	13.19	3.93	7.37	10.57	15.79	9.98	8.22	10.77	9.63	11.08	12.68	8.04
Na_2O	1.54	1.79	3.58	3.39	3.38	1.24	3.50	2.43	2.33	3.89	1.71	1.24	3.43
K_2O	0.34	0.56	0.99	0.72	0.43	0.09	1.27	1.99	0.35	0.62	1.3	1.3	3.33
Sum	**100.0**	**100.0**	**100.0**	**100.0**	**100.0**	**100.0**	**100.0**	**100.0**	**100.0**	**100.0**	**100.0**	**100.0**	**100.0**
La	0.88	1.89	8.59	5.61	6.22	0.9	25	32.5	22.8	23.6			26.80
Ce	3.18	5.56	20.7	14.4	13	1.7	52	57	48.8	47.4			61.60
Pr	0.66	0.97	2.8	2.2	1.63	0.25	3.86	6.29	6.12	6.33			7.51
Nd	4.52	5.44	12.7	10.3	7.11	1.1	29	24.3	26.2	24.2			30.80
Sm	1.93	2.14	3.66	3.11	2	0.4	5.53	5	5.3	4.8			6.31
Eu	0.73	0.90	1.04	1.04	0.84	0.3	1.6	1.56	1.39	1.57			1.60
Gd	3.03	2.95	4.41	2.96	2	0.4	3.33	4.3	4.2	3.8			4.99
Tb	0.46	0.49	0.78	0.49	0.32	< 0.1		0.7	0.6	0.5			0.76
Dy	2.99	3.01	5.36	3.3	1.99	0.4	0.65	3.6	3.1	3			3.62
Ho	0.58	0.6	1.09	0.68	0.42	< 0.1	0.65	0.7	0.6	0.5			0.66
Er	1.7	1.61	3.31	1.81	1.26	0.2	1.57	1.8	1.5	1.5			2.04
Tm	0.22	0.23	0.49	0.277	0.19	< 0.05		0.25	0.2	0.21			0.27
Yb	1.31	1.4	3.34	1.75	1.28	0.2	1.61	1.6	1.2	1.3			1.98
Lu	0.18	0.20	0.54	0.32	0.21	< 0.04	0.25	0.23	0.16	0.17			0.30
Cs	0.3	1.1	0.3	0.3	0.6	0.7		0.9	< 0.5	< 0.5			
Rb	4	11	2	20	10	40		65	5	7			
Ba	56	70	203	205	168	0.5	390	404	241	282			
Th	0.05	0.19	3.57	0.51	0.99	0.1	5.92	6.5	5.3	8.1			
U	0.05	0.28	1.18	0.64	0.69	0.1		1.6	1.1	2.2			
Nb	0.6	0.8	1.7	2.7	0.7	2	8.44	17	6	10			
Ta	0.01	0.04	0.12	0.51	0.01	0.1	0.37	1.5	0.4	0.8			
Pb	5	5	5	6	5	5		< 5	< 5	< 5			
Sr	383	319	206	444	776	22	645	386	287	358			
Zr	13	15	146	89	30	5	58	120	91	109			
Hf	0.4	0.5	4.3	2.1	0.8	0.2	4.2	2.9	2.5	2.7			
Y	15	15.2	31.9	19.1	11.3	1	21	17	15	14			

* 40Ar/39Ar in amphibole; ** U-Pb in zircon

Table 4. New Sm-Nd and Rb-Sr isotopes data for samples of the Fuegian Batholith and lamprophyre. Also, the isotopic composition of different plutonic rocks belonging to the Southern Patagonian Batholith (Hervé et al., 2007) is shown.

Sample	Locality	Lithology	Age	Sm (ppm)	Nd (ppm)	147/144	143/144	143/144i	εNd	Tchur	Tdm	DP	Tdm2	Rb	Sr	Rb/Srwt	87Rb/86Sr	87Sr/86Sr	87/86i	eps (Sr)	TBulk
13AP01-30	Fuegian Batholith	Hornblendite	100	1.93	4.52	0.2258	0.512128	0.512126	1.8973429995	341.2222	-14118.1330	19095.579	592.037	4.0000	383.0000	0.0010	0.030	0.704	0.704	-5.4475	6033.2280
13AP01-31	Fuegian Batholith	Hblpegmatite	100	2.14	5.44	0.2238	0.512129	0.512127	3.73[illegible]61	803596	-25229.10106	16522.2999	4583.3557	11.0000	319.0000	0.034	0.100	0.704	0.704	-6.3866	-1926.9334
13APO1-41	Fuegian Batholith	Hbltonalite	120	3.66	12.7	0.1[illegible]	0.512128	0.512126	3.183862305	-9988.6669	9888.8827	17511.8733	5133.8336	21.0000	206.0000	0.1022	0.295	0.704	0.704	-6.9399	-433.0065
FC1811	Fuegian Batholith	Px-Hblgabbro	60	2	7.11	0.1170	0.512129	0.512128	5.037603262	-14334.8099	617.5537	13999.81616	333.8881	10.0000	776.0000	0.0013	0.037	0.704	0.704	-10.8511	12044.00533
FC1854	Fuegian Batholith	Hbltonalite	120	3.11	10.3	0.1183	0.512128	0.512127	3.947413725	-20955.8400	1019.9885	16399.89696	458.4435	20.0000	444.0000	0.0445	0.130	0.704	0.704	-5.4133	-4602.2588
ST02	Fuegia	Lamp	75	2.47	12.1	0.1	0.5	0.5	3.99	-3	44	50	42	3.	25	0.0	0.03	0.7	0.	0.	54.

25B17	n Batholith	rophyre		4288932	33656464	23	128	127	83598893	52.8002	8.6996	2.0441	0.6653	2522	3.3995	13	7	04	704	197	174

Table 5. Representative major element composition (wt.%) of amphibole (cations are normalized to 23 oxygens).

Sample	13AP011-30	13AP011-30	13AP011-30	13AP011-30	13AP011-30	13AP011-30	MT2889	MT2889	MT2889	MT2889	MT2889	MT2889	AA14418	AA14418	AA14418	AA14418	AA14418	FC18111	FC18111	FC18111	MT1112	MT1112	MT1112	MT1112	MT1112	TN07113C	TN07113C	TN07113C	TN07113C	TN07113C	TN07113C	FC18554	FC18554	FC18554	FC18554	FC18554	FC18554
Locality	FB	FB	FB	FB	FB	FB	UP	UP	UP	UP	UP	UP	FB	FB	FB	FB	FB	FB	FB	FB	UP	UP	UP	UP	UP	TC	TC	TC	TC	TC	TC	FB	FB	FB	FB	FB	FB
Lithology	Hornblende endidite	Hornblende endidite	Hornblende endidite	Hornblende endidite	Hornblende endidite	Hornblende endidite	Hornblende endidite	Hornblende endidite	Hornblende endidite	Hornblende endidite	Hornblende endidite	Hornblende endidite	Gabbro	Gabbro	Gabbro	Gabbro	Gabbro	Gabbro	Gabbro	Gabbro	Monzodiorite	Monzodiorite	Monzodiorite	Monzodiorite	Monzodiorite	Lamprophyre	Lamprophyre	Lamprophyre	Lamprophyre	Lamprophyre	Lamprophyre	Tonalite	Tonalite	Tonalite	Tonalite	Tonalite	Tonalite
SiO_2	40.552	40.663	40.228	41.113	40.178	40.081	39	38.995	40.443	40.113	39.881	40.007	48.568	46.173	45.371	46.929	51.468	48.086	44.979	46.896	41.366	40.908	41.146	40.93	40.583	42.124	42.039	43.136	43.537	41.917	40.786	40.603	45.555	47.02	45.291	44.508	44.467	44.967
TiO_2	1.776	1.771	1.777	1.662	1.555	1.578	1.98	1.995	1.776	1.987	1.981	1.994	0.387	0.517	0.799	0.563	0.368	1.527	2.418	1.991	1.525	1.542	1.56	1.507	1.599	1.341	1.715	1.057	1.318	1.806	1.873	1.779	0.935	0.699	1.006	0.988	0.875	0.908
Al	14	14	15	14	15	14	13	13	12	13	14	13	6.	8.	8.	7.	4.	5.	8.	7.	10	11	10	10	11	10	13	11	12	13	13	13	9.	8.	9.	10	10	10

$_2O_3$	.85	.78	.21	.51	.2	.98	.32	.32	.23	.8	.07	.11	688	095	592	355	174	296	498
Cr_2O_3	<0.0	<0.0	<0.0	<0.0	<0.0	<0.0	0.02	0.02	0.01	0.02	0.01	0.01	<0.0	<0.0	<0.0	<0.0	<0.0	0.014	<0.0
FeOT	10.71	10.69	10.66	10.3	9.87	10.53	12.67	13.13	12.67	11.02	10.82	13.12	12.333	11.577	11.911	11.129	11.876	9.726	11.332
MnO	0.08	0.19	0.13	0.15	0.16	0.15	0.205	0.23	0.21	0.11	0.15	0.21	0.238	0.374	0.277	0.283	0.297	0.233	0.204
MgO	14.23	14.52	14.13	14.14	14.54	14.16	12.62	12.47	13.4	13.83	13.53	12.4	14.473	14.16	13.706	13.92	15.911	15.854	15.275
CaO	11.92	11.85	12.02	12.15	11.97	11.98	12.18	12.02	12.39	12.55	12.49	12.23	11.817	10.951	10.782	11.[illegible]5	11.527	15.362	11.712
Na_2O	2.24	2.27	2.27	2.21	2.1	2.25	2.32	2.36	2.05	2.2	2.25	2.15	0.624	0.873	0.951	0.777	0.345	0.745	1.69
K_2O	0.5	0.52	0.5	0.46	0.39	0.46	1.43	1.58	1.49	1.8	1.88	1.53	0.158	0.259	0.357	0.21	0.086	0.463	0.567
Sum	96.81	97.16	96.98	96.68	96.56	97.1	95.77	96.09	96.63	97.33	96.98	96.75	95.286	92.979	92.696	92.316	96.052	97.306	96.675
Si	5.909	5.897	5.868	6.011	5.924	5.933	5.913	5.902	6.050	5.948	5.934	6.020	7.143	6.942	6.865	7.112	7.477	6.987	6.586
A	2	2	2	1	2	2	2	2	1	2	2	1	0	1	1	0	0	0	1

$_2O_3$	35	.734	.029	.928	.907	.237	.394	.358	.96	.022	.419	.529	.165	583	601	749	.992	.875	.44
Cr_2O_3	0.018	<0.0	0.009	0.009	0.011	0.016	0.027	0.443	0.031	0.076	0.25	0.057	0.199	<0.0	<0.0	0.013	0.004	0.006	0.025
FeOT	11.095	17.983	18.411	17.907	17.792	17.82	17.29[illegible]	8.155	10.915	9.205	8.687	8.707	8.619	14.192	13.532	14.303	14.19	15.23	14.573
MnO	0.222	0.783	0.826	0.754	0.75	0.7[illegible]5	0.73	0.086	0.174	0.201	0.12	0.136	0.104	0.451	0.534	0.555	0.502	0.509	0.546
MgO	16.[illegible]86	8.698	8.331	8.554	8.365	8.311	9.148	16.525	14.954	16.643	16.371	15.927	16.202	11.566	12.417	11.505	11.144	10.648	11.079
CaO	11.645	11.745	11.676	11.71	11.5	11.757	11.674	12.244	11.959	11.66	12.135	11.927	12.04	11.466	11.444	11.461	11.27	11.54	11.417
Na_2O	1.377	1.335	1.346	1.424	1.199	1.356	1.265	2.39	1.926	2.303	2.39	2.318	2.41	1.005	0.914	1.081	1.207	1.204	1.16
K_2O	0.615	1.686	1.69	1.664	1.68	1.783	1.476	1.02	0.661	0.641	0.866	1.146	0.912	0.371	0.282	0.365	0.476	0.527	0.43
Sum	97.295	95.855	95.768	95.656	94.641	95.237	95.47	97.975	96.773	97.606	97.961	96.406	96.033	95.124	95.443	95.329	95.281	95.881	95.545
Si	6.791	6.425	6.374	6.411	6.432	6.363	6.525	6.034	6.287	6.237	6.013	5.964	5.950	6.838	6.988	6.795	6.680	6.679	6.744
A	1	1	1	1	1	1	1	1	1	1	1	2	2	1	1	1	1	1	1

Al iv	.091	.103	.131	.989	.076	.067	.087	.098	.949	.052	.066	.979	.857	.058	.135	.888	.523	.907	.414	.209	.575	.626	.589	.568	.637	.475	.966	.713	.763	.987	.036	.050	.162	.012	.205	.320	.321	.256
Ti	0.193	0.187	0.194	0.178	0.170	0.194	0.225	0.227	0.198	0.208	0.222	0.219	0.043	0.058	0.091	0.064	0.040	0.167	0.266	0.217	0.178	0.181	0.183	0.178	0.189	0.156	0.185	0.116	0.142	0.195	0.206	0.196	0.106	0.078	0.113	0.112	0.099	0.102
Al vi	0.462	0.425	0.480	0.510	0.528	0.501	0.294	0.282	0.208	0.359	0.406	0.342	0.302	0.376	0.397	0.426	0.192	0.000	0.053	0.046	0.390	0.399	0.418	0.453	0.439	0.422	0.294	0.342	0.267	0.282	0.296	0.224	0.534	0.495	0.518	0.624	0.603	0.589
Cr	0.000	0.000	0.000	0.000	0.000	0.000	0.002	0.003	0.001	0.002	0.001	0.001	0.000	0.000	0.000	0.000	0.000	0.002	0.000	0.002	0.000	0.001	0.001	0.0[illegible]1	0.00[illegible]	0.003	0.050	0.004	0.009	0.028	0.007	0.023	0.000	0.000	0.002	0.000	0.001	0.003
Fe+2	1.325	1.319	1.318	1.273	1.217	1.298	1.623	1.679	1.602	1.376	1.355	1.660	1.074	0.880	0.936	1.083	1.088	0.887	0.91[illegible]	0.86[illegible]	2.[illegible]5	2.223	2.[illegible]41	2.215	2.260	2.107	0.411	0.680	0.358	0.387	0.430	0.345	1.541	1.824	1.546	1.513	1.687	1.591
Mn	0.009	0.023	0.016	0.018	0.020	0.019	0.027	0.030	0.027	0.014	0.019	0.027	0.030	0.048	0.036	0.0[illegible]7	0.0[illegible]7	0.029	0.026	0.027	0.103	0.109	0.100	0.100	0.103	0.096	0.011	0.022	0.025	0.015	0.017	0.013	0.058	0.250	0.071	0.064	0.065	0.070
Mg	3.118	3.172	3.094	3.096	3.177	3.089	2.878	2.842	3.019	3.075	3.021	2.796	3.17[illegible]	3.173	3.091	3.144	3.445	3.433	3.334	3.472	2.014	1.935	1.987	1.959	1.942	2.112	3.536	3.249	3.554	3.501	3.471	3.539	2.558	2.751	2.573	2.493	2.384	2.476
Ca	1.878	1.861	1.891	1.913	1.880	1.880	1.997	1.970	2.007	2.007	2.005	1.982	1.862	1.764	1.740	1.810	1.794	2.000	1.837	1.807	1.955	1.949	1.955	1.936	1.975	1.937	1.883	1.868	1.790	1.865	1.869	1.890	1.844	1.822	1.842	1.812	1.857	1.834
Na	0.561	0.555	0.574	0.576	0.519	0.562	0.671	0.667	0.587	0.627	0.648	0.609	0.104	0.129	0.141	0.120	0.049	0.210	0.383	0.301	0.378	0.379	0.406	0.331	0.399	0.346	0.603	0.474	0.528	0.593	0.587	0.626	0.203	0.918	0.228	0.237	0.272	0.239
K	0.093	0.097	0.094	0.087	0.074	0.086	0.279	0.309	0.288	0.342	0.360	0.295	0.030	0.050	0.070	0.041	0.016	0.086	0.107	0.115	0.335	0.337	0.331	0.338	0.357	0.293	0.189	0.125	0.119	0.161	0.217	0.173	0.071	0.186	0.070	0.091	0.101	0.082
Fe+3	0.662	0.737	0.664	0.511	0.689	0.600	0.404	0.411	0.481	0.311	0.212	0.311	0.409	0.512	0.484	0.283	0.234	0.294	0.438	0.397	0.141	0.176	0.092	0.123	0.077	0.133	0.524	0.610	0.670	0.607	0.591	0.673	0.232	2.946	0.248	0.258	0.225	0.237
Mg	0.	0.	0.	0.	0.	0.	0.	0.	0.	0.	0.	0.	0.	0.	0.	0.	0.	0.	0.	0.	0.	0.	0.	0.	0.	0.	0.	0.	0.	0.	0.	0.	0.	0.	0.	0.	0.	0.

-no	70	71	70	71	72	70	64	63	65	69	69	63	75	78	77	74	76	79	79	80	48	47	47	47	46	50	90	83	91	90	89	91	63	60	62	62	59	61

Table 6. Trace and rare earth element composition (ppm) of amphibole from selected samples.

Sample	Locality	Lithology		La	Ce	Pr
13APO11-30	FB	Hornblende endidite		0.696	2.820	0.67
13APO11-30	FB	Hornblende endidite		0.991	2.931	0.70
13APO11-30	FB	Hornblende endidite		1.102	3.654	0.81
13APO11-30	FB	Hornblende endidite		1.159	3.649	0.90
13APO11-30	FB	Hornblende endidite		0.731	3.196	0.78
13APO11-30	FB	Hornblende endidite		0.884	3.460	0.80
MT289	UP	Hornblende endidite		9.840	28.900	4.96
MT289	UP	Hornblende endidite		12.700	36.300	5.69
MT289	UP	Hornblende endidite		11.700	34.800	5.76
MT289	UP	Hornblende endidite		12.200	34.300	5.23
MT289	UP	Hornblende endidite		14.800	41.900	6.30
MT289	UP	Hornblende endidite		15.500	40.500	6.39
AA1441	FB	Gabbro		0.884	3.868	0.86
AA1441	FB	Gabbro		0.774	3.716	0.81
AA1441	FB	Gabbro		0.926	4.075	0.86
AA1441	FB	Gabbro		1.031	4.322	0.92
AA1441	FB	Gabbro		0.679	2.626	0.54
AA1441	FB	Gabbro		0.869	3.737	0.74
AA1441	FB	Gabbro		0.761	3.189	0.70
FC1811	FB	Gabbro		1.871	8.244	1.84
FC1811	FB	Gabbro		0.654	2.304	0.49
FC1811	FB	Gabbro		2.176	9.274	2.11
FC1811	FB	Gabbro		0.713	2.540	0.49
FC1811	FB	Gabbro		10.785	42.867	8.47
MT112	UP	Monzodiorite		15.784	42.346	5.74
MT112	UP	Monzodiorite		17.683	40.599	5.61
MT112	UP	Monzodiorite		18.332	37.608	4.25
MT112	UP	Monzodiorite		11.087	26.583	3.53
MT112	UP	Monzodiorite		16.789	43.004	6.13
MT112	UP	Monzodiorite		22.840	58.472	8.01
TN07133C	TC	Lamprophyre		4.232	14.309	2.72
TN07133C	TC	Lamprophyre		4.119	14.360	2.76
TN07133C	TC	Lamprophyre		4.122	14.910	3.07
TN07133C	TC	Lamprophyre		3.286	12.626	2.70
TN07133C	TC	Lamprophyre		4.062	15.933	3.25
TN07133C	TC	Lamprophyre		3.352	12.603	2.55
FC18541	FB	Tonalite		4.555	23.742	5.51
FC18541	FB	Tonalite		6.592	30.095	6.24
FC18541	FB	Tonalite		6.715	32.538	6.91
FC18541	FB	Tonalite		4.861	21.962	4.23
FC18541	FB	Tonalite		4.829	21.155	3.97
FC18541	FB	Tonalite		6.257	25.854	4.74

	7	2	0	3	5	2	0	0	0	0	0	0	5	0	7	9	8	0	7	3	1	5	7	2	2	0	2	5	8	7	1	9	6	4	7	0	1	2	5	3	8	7
Nd	5.089	5.487	5.715	6.388	6.252	6.632	26.400	31.200	28.200	28.500	31.900	32.800	5.899	5.698	6.589	7.071	4.445	5.169	4.882	12.254	3.026	14.883	3.723	53.976	26.500	25.922	17.269	16.588	29.173	36.993	17.552	17.546	18.265	16.818	18.581	16.406	30.233	37.135	45.136	24.133	24.606	26.348
Sm	2.278	2.518	2.633	3.270	3.094	3.226	6.980	7.690	6.990	7.090	7.660	7.020	2.637	2.774	3.791	3.395	2.442	2.055	1.952	4.743	1.167	6.421	1.675	18.129	7.036	6.154	3.167	3.894	7.194	8.390	5.016	5.102	5.832	5.439	6.467	5.568	11.107	13.423	17.381	7.720	8.742	8.777
Eu	0.833	0.873	0.889	1.063	1.091	1.025	1.880	2.180	2.040	2.040	2.310	2.270	0.616	0.599	0.753	0.771	0.480	0.778	0.295	0.768	0.219	0.698	0.228	3.920	1.848	1.531	1.175	1.313	1.964	2.345	1.563	1.526	1.538	1.659	1.878	1.498	2.598	3.040	3.771	2.062	2.088	1.859
Gd	2.989	3.332	3.387	3.884	4.211	3.773	5.450	6.400	5.660	5.280	5.860	5.880	4.326	4.273	4.651	4.237	3.213	3.270	2.717	5.996	1.294	6.855	2.017	21.369	5.925	5.286	2.828	3.673	5.842	7.705	5.570	5.075	4.706	5.884	7.801	5.149	11.983	14.347	19.783	8.811	9.368	8.409
Tb	0.551	0.528	0.599	0.704	0.668	0.698	0.753	0.801	0.775	0.660	0.705	0.743	0.737	0.761	0.881	0.822	0.592	0.552	0.517	0.069	0.283	1.284	0.381	3.511	0.837	0.790	0.412	0.491	0.877	1.081	0.812	0.777	0.737	0.755	0.979	0.755	1.978	2.432	3.302	1.498	1.570	1.345
Dy	3.208	3.402	3.639	4.347	4.234	4.152	3.360	3.890	3.550	3.550	4.190	3.730	4.764	4.252	5.548	5.489	3.671	3.591	3.578	6.824	1.995	7.740	2.494	22.131	4.921	4.789	2.352	3.050	5.306	6.712	4.419	4.000	4.264	4.387	5.535	4.260	13.568	16.386	23.213	9.854	10.791	8.863
Ho	0.634	0.650	0.731	0.867	0.942	0.931	0.625	0.762	0.678	0.637	0.797	0.308	1.036	0.928	1.120	1.024	0.755	0.752	0.847	1.472	0.446	1.700	0.663	4.923	0.965	0.933	0.533	0.609	1.181	1.238	0.864	0.824	0.756	0.838	1.126	0.742	2.758	3.307	4.973	2.080	2.209	1.911
Er	1.980	1.977	2.217	2.607	2.441	2.575	1.480	2.060	1.910	1.630	2.050	2.160	2.955	2.674	3.163	3.033	2.071	1.943	2.648	4.441	1.485	5.128	2.111	14.483	2.880	3.176	1.888	2.119	3.639	3.851	2.310	2.178	2.193	2.094	2.797	2.196	8.368	10.189	15.416	6.626	6.932	6.177
Tm	0.230	0.245	0.269	0.353	0.327	0.381	0.202	0.246	0.270	0.224	0.245	0.347	0.437	0.372	0.435	0.407	0.272	0.293	0.434	0.591	0.279	0.710	0.328	2.136	0.501	0.401	0.299	0.351	0.537	0.606	0.256	0.344	0.262	0.288	0.364	0.266	1.292	1.494	2.231	1.025	1.128	0.925
Yb	1.40	1.54	1.54	2.03	1.92	2.03	1.29	1.53	1.61	1.66	1.87	1.77	2.69	2.46	2.69	2.58	1.79	1.67	2.90	3.80	2.04	4.37	2.24	13.6	3.49	3.22	1.96	2.74	3.89	3.96	1.67	1.82	1.85	1.58	2.26	1.56	8.43	10.0	14.4	6.82	7.45	6.20

	9	3	4	0	1	1	0	0	0	0	0	0	7	1
Lu	0.178	0.231	0.239	0.348	0.285	0.285	0.182	0.258	0.208	0.209	0.260	0.273	0.392	0.381
Rb	1.801	1.518	2.535	1.761	1.584	2.024	8.620	9.120	9.820	6.780	7.040	8.990	0.213	0.264
Ba	49.178	48.394	57.910	60.400	51.827	59.857	291.000	316.000	267.000	254.000	388.000	415.000	1.956	1.223
Nb	0.762	0.827	1.006	0.907	0.829	0.952	1.560	2.980	2.380	2.970	3.120	3.270	0.068	0.048
Sr	206.102	223.017	191.148	259.820	259.140	220.316	799.000	727.000	655.000	670.000	723.000	722.000	13.278	11.448
Zr	12.529	13.637	15.483	15.265	12.308	15.278	46.550	61.400	50.850	52.950	67.600	72.900	12.700	10.575
Ti	13497.340	13412.240	12497.630	14363.270	14170.710	13996.220	12600.000	12300.000	11000.000	10500.000	12200.000	13900.000	3585.191	2908.581
Y	21.250	21.777	21.469	22.624	23.668	23.878	15.700	18.700	16.600	17.400	17.500	19.000	23.016	21.415

	9	7	4	7	4	6	2	8	3	89	2	5	4	4
Lu	0.420	0.369	0.214	0.241	0.439	0.581	0.355	0.660	0.437	2.058	0.588	0.572	0.486	0.480
Rb	0.228	0.288	0.205	0.535	-0.007	0.337	0.112	0.163	0.127	1.702	10.883	9.941	6.472	8.980
Ba	1.796	2.903	1.097	3.892	0.706	2.046	0.314	2.907	1.322	141.392	67.703	64.18[illegible]	16.755	21.880
Nb	0.056	0.036	0.045	0.050	0.016	0.029	0.025	0.301	0.018	5.458	4.836	5.326	2.546	2.419
Sr	14.131	12.002	9.235	9.895	11.986	14.843	12.065	13.048	10.958	122.906	133.004	128.342	81.687	92.771
Zr	11.250	12.380	10.563	8.990	17.660	31.254	5.484	45.279	11.520	177.603	56.318	55.892	39.657	37.069
Ti	3707.310	2643.701	3118.022	2578.489	1101.662	1638.319	990.779	2610.398	925.516	14973.150	9941.578	9927.348	7389.244	7645.378
Y	25.353	24.117	17.509	15.442	20.778	33.846	11.302	41.784	14.993	121.409	24.986	26.898	14.138	17.227

	1	0	5	7	2	6	6	9	9	01	33	8	5	7
Lu	0.630	0.715	0.212	0.248	0.283	0.236	0.326	0.229	1.184	1.379	2.115	1.119	1.109	1.078
Rb	12.193	9.992	3.039	3.297	3.476	3.747	3.925	3.395	0.708	0.823	1.802	24.241	7.536	0.940
Ba	51.943	111.247	141.792	122.000	122.292	159.248	161.703	158.023	15.675	16.978	17.013	52.473	107.533	15.622
Nb	4.688	7.621	2.811	2.499	2.735	2.486	2.626	2.415	2.394	2.855	12.073	2.113	2.063	2.048
Sr	138.865	163.329	383.843	368.621	375.251	429.728	474.687	401.665	17.539	41.976	21.853	275.731	102.019	23.285
Zr	56.302	67.987	35.913	38.931	41.315	33.663	38.812	32.669	35.299	38.268	51.391	19.946	19.767	19.901
Ti	10446.270	10795.150	10556.080	8458.306	8095.611	10783.760	12283.190	10600.950	4826.481	5488.026	16138.590	3185.790	2814.418	2856.414
Y	27.875	32.294	19.629	19.109	19.455	18.549	22.743	17.523	71.447	82.504	117.515	52.931	57.655	49.875

Yb	1.409	1.543	1.544	2.030	1.921	2.031	1.290	1.530	1.610	1.660	1.870	1.770	2.697	2.461	2.699	2.587	1.794	1.677	2.904	3.806	2.042	4.378	2.243	13.689	3.492	3.225	1.964	2.744	3.891	3.960	1.675	1.827	1.852	1.586	2.266	1.569	8.439	10.001	14.433	6.828	7.455	6.207
V	390.346	339.473	426.092	501.879	490.806	490.804	491.000	534.000	543.000	509.000	648.000	675.000	438.604	362.471	434.110	396.153	352.566	340.693	69.659	131.991	32.323	154.329	73.609	473.581	479.732	468.962	368.672	457.835	540.561	489.973	502.524	435.026	434.633	510.173	609.328	486.304	352.709	306.095	491.658	249.916	406.716	414.647
Cr	95.119	83.194	89.896	99.915	147.511	118.108	38.300	21.000	20.200	21.100	24.300	23.600	27.378	20.752	24.975	26.920	22.676	22.087	1.114	1.820	0.907	0.334	0.840	2.962	15.027	9.331	1.899	5.242	11.141	9.138	1647.228	1301.779	1331.073	1525.866	2926.940	2369.464	14.034	8.663	24.327	24.532	35.223	23.967
Ni	27.805	32.381	25.709	28.522	26.114	28.512	32.600	35.100	32.200	32.200	35.800	36.900	45.156	41.768	49.949	55.084	38.590	52.636	18.232	14.282	22.687	13.298	20.363	21.626	20.722	25.896	25.118	24.604	24.647	22.689	166.487	446.331	230.803	290.868	264.180	259.306	26.322	22.633	26.219	16.419	23.051	21.568
Nb	0.762	0.827	1.006	0.907	0.829	0.952	1.560	2.980	2.380	2.970	3.120	3.270	0.068	0.043	0.056	0.036	0.045	0.050	0.016	0.029	0.025	0.301	0.018	5.458	4.836	5.326	2.546	2.419	4.688	7.621	2.811	2.499	2.735	2.486	2.626	2.415	2.394	2.855	12.073	2.113	2.063	2.048
Cs	0.124	-0.005	0.037	0.037	0.025	0.047	0.050	0.068	0.164	0.075	0.009	0.254	0.000	-0.006	0.003	0.005	-0.019	0.003	0.045	0.007	0.025	0.060	0.079	0.035	0.021	0.031	0.040	0.061	0.000	0.018	0.017	0.016	0.064	-0.003	0.016	0.017	0.008	0.058	0.056	0.990	0.164	0.035
Ba	49.178	48.394	57.910	60.400	51.827	59.857	291.000	316.000	267.000	254.000	388.000	415.000	1.956	1.223	1.796	2.903	1.097	3.892	0.706	2.046	0.314	2.907	1.322	141.392	67.708	64.186	16.755	21.880	51.943	111.247	141.792	122.002	122.292	159.248	161.703	158.023	15.675	16.978	17.013	52.473	107.533	15.622
Hf	0.461	0.475	0.558	0.672	0.594	0.620	2.280	2.570	2.360	2.210	2.660	2.810	0.902	0.966	0.934	0.837	0.784	0.551	0.837	1.931	0.196	2.174	0.686	8.571	3.213	3.223	3.228	3.166	3.390	3.731	1.749	2.004	2.040	1.891	2.231	1.744	2.482	2.772	4.418	1.517	1.652	1.716

Electronic Annex 1. Full data of amphibole compositions.

Highlights

- Magma evolution in crustal plumbing systems
- Amphibole geochemistry as a proxy for magmatic processes in subduction zones
- Hornblendites and their link with deep-seated crustal physicochemical processes
- Origin of primitive hydrous magmas in steep and flat subduction subduction zones

Declaration of interests

The authors declare that they have no known competing financial interests or personal relationships that could have appeared to influence the work reported in this paper.

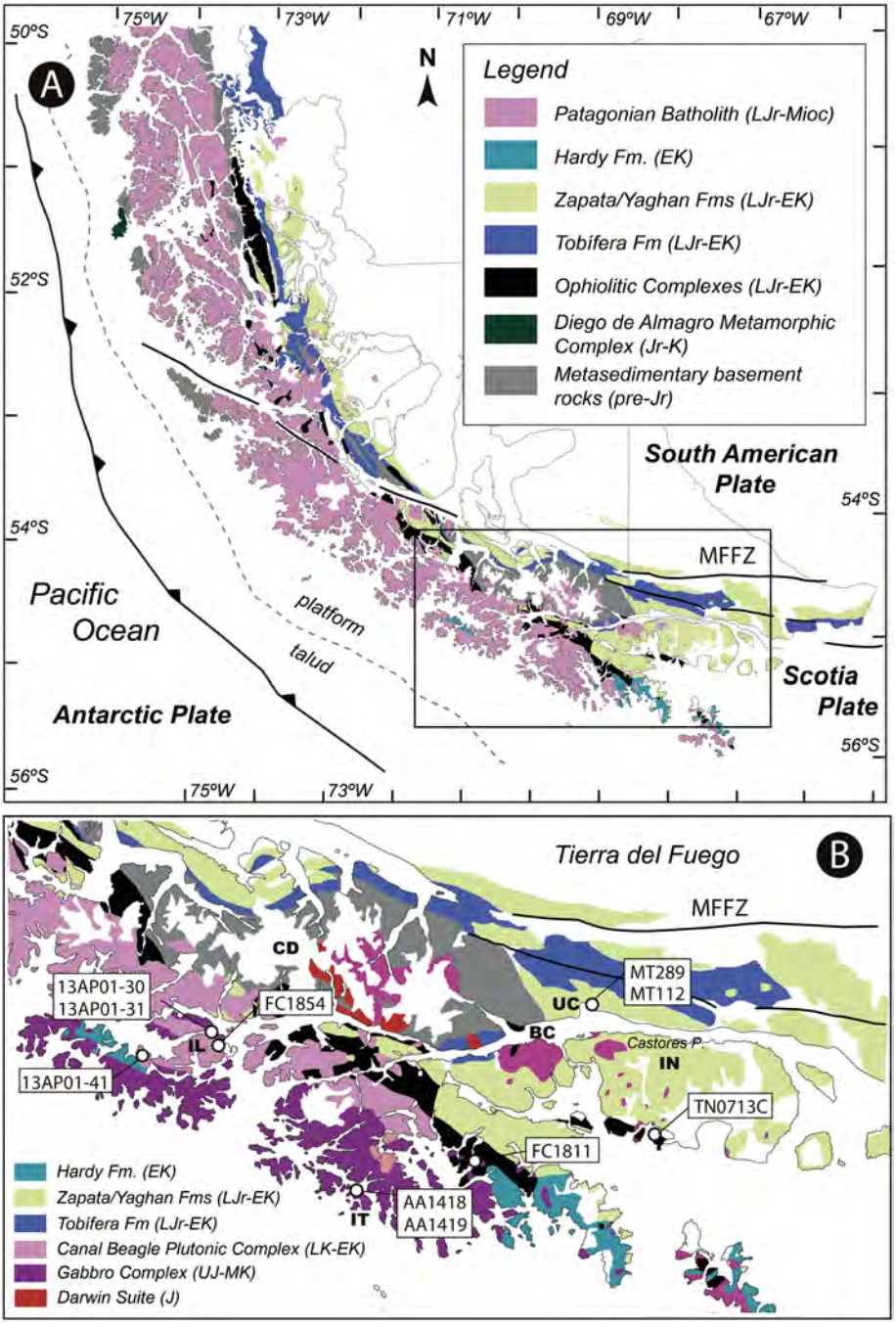
A
75°W
73°W
71°W
69°W
67°W
50°S
52°S
54°S
56°S
N
Legend
Patagonian Batholith (LJr-Mioc)
Hardy Fm. (EK)
Zapata/Yaghan Fms (LJr-EK)
Tobifera Fm (LJr-EK)
Ophiolitic Complexes (LJr-EK)
Diego de Almagro Metamorphic Complex (Jr-K)
Metasedimentary basement rocks (pre-Jr)
South American Plate
MFFZ
Pacific Ocean
platform
talud
Antarctic Plate
Scotia Plate
B
Tierra del Fuego
MFFZ
CD
13AP01-30
13AP01-31
FC1854
IL
13AP01-41
MT289
MT112
UC
BC
Castores P.
IN
TN0713C
FC1811
AA1418
AA1419
IT
Hardy Fm. (EK)
Zapata/Yaghan Fms (LJr-EK)
Tobifera Fm (LJr-EK)
Canal Beagle Plutonic Complex (LK-EK)
Gabbro Complex (UJ-MK)
Darwin Suite (J)

Figure 1

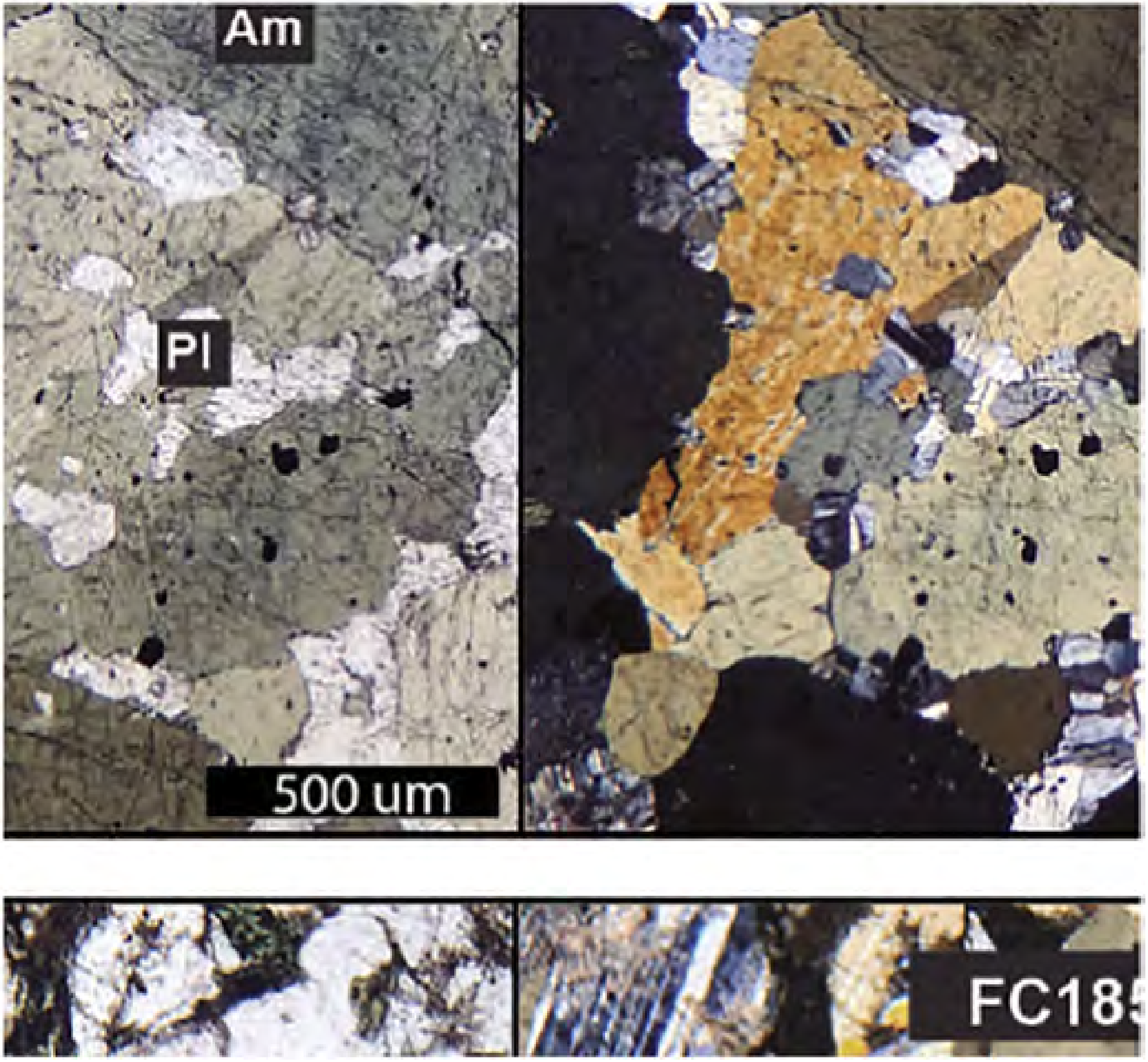

Figure 2

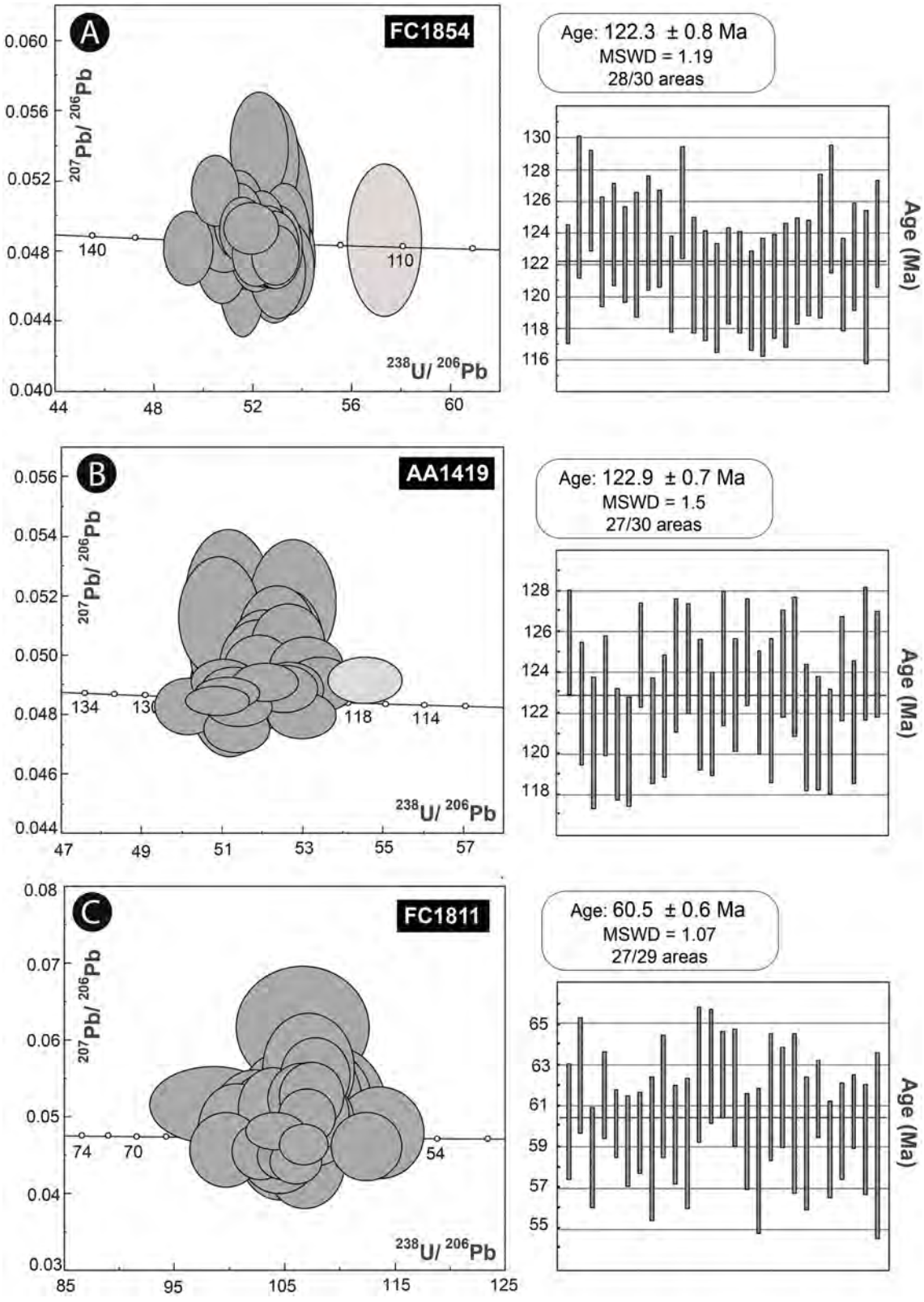
A
FC1854
$^{207}Pb/^{206}Pb$
$^{238}U/^{206}Pb$
140
110
Age: 122.3 ± 0.8 Ma
MSWD = 1.19
28/30 areas
Age (Ma)
B
AA1419
134
118
114
Age: 122.9 ± 0.7 Ma
MSWD = 1.5
27/30 areas
C
FC1811
74
70
54
Age: 60.5 ± 0.6 Ma
MSWD = 1.07
27/29 areas

Figure 3

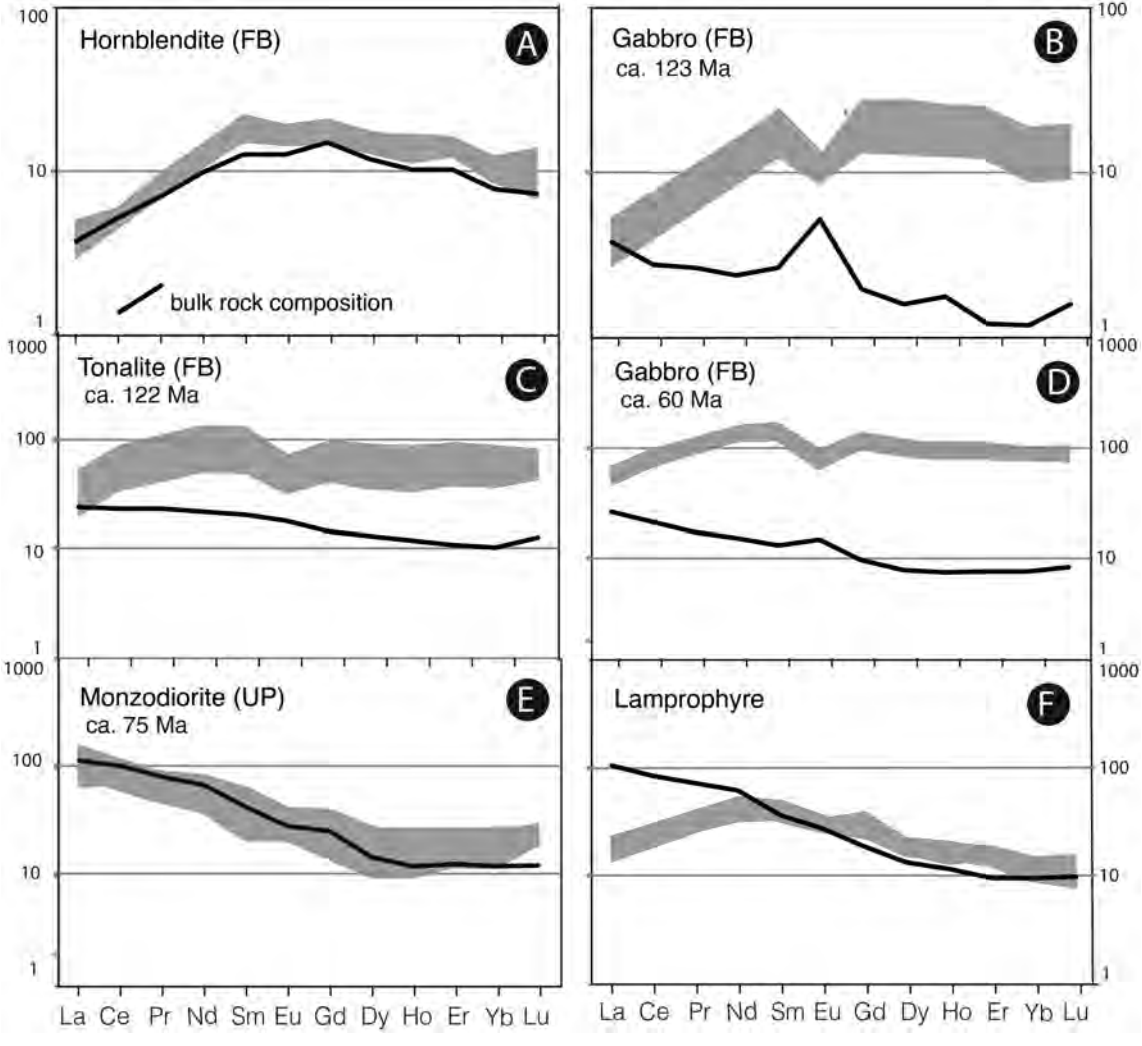
Hornblendite (FB)
A
bulk rock composition
Gabbro (FB)
ca. 123 Ma
B
Tonalite (FB)
ca. 122 Ma
C
Gabbro (FB)
ca. 60 Ma
D
Monzodiorite (UP)
ca. 75 Ma
E
Lamprophyre
F
100
10
1
1000
La Ce Pr Nd Sm Eu Gd Dy Ho Er Yb Lu

Figure 4

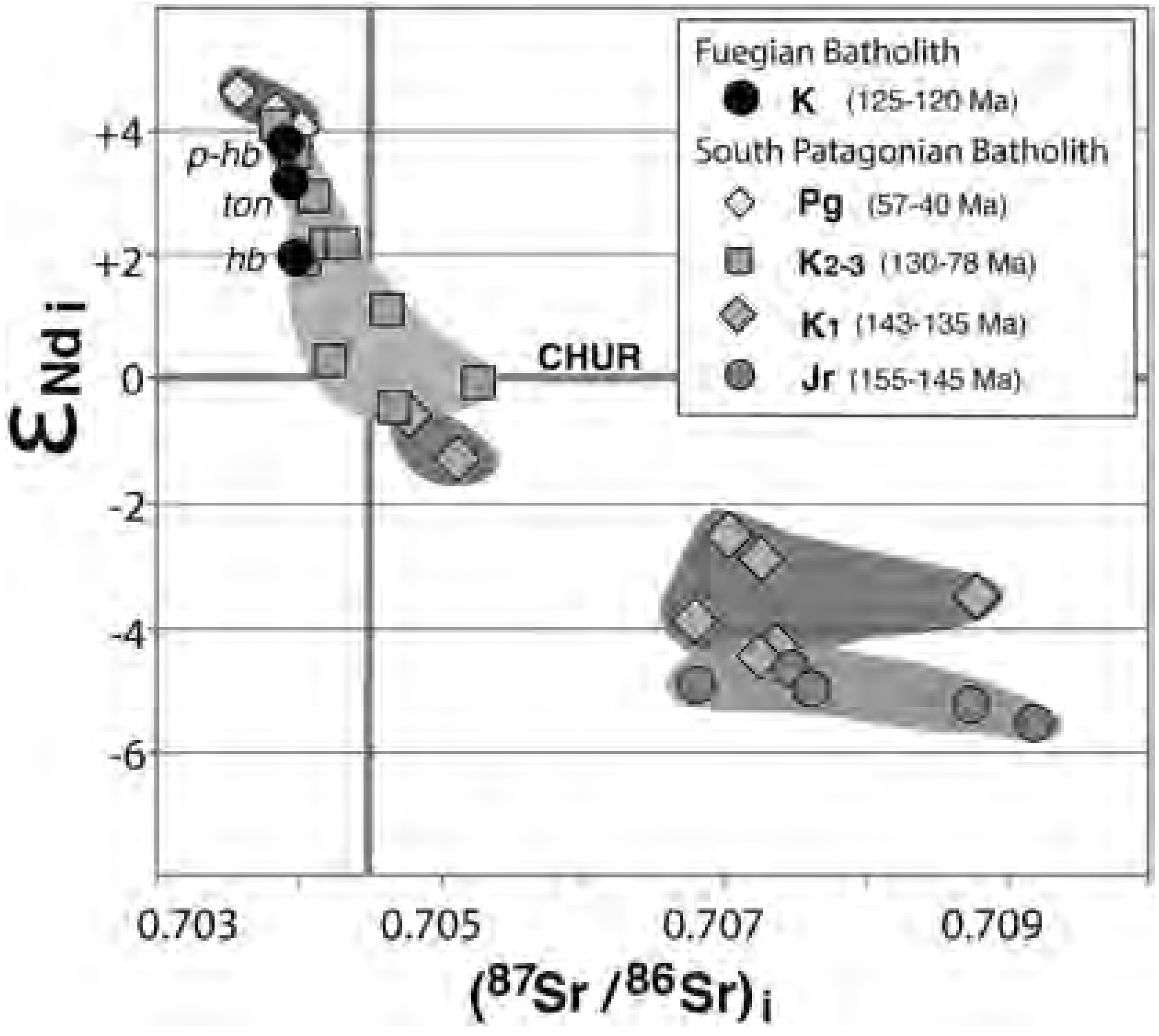
Fuegian Batholith
K (125-120 Ma)
South Patagonian Batholith
Pg (57-40 Ma)
K2-3 (130-78 Ma)
K1 (143-135 Ma)
Jr (155-145 Ma)
p-hb
ton
hb
CHUR
+4
+2
0
-2
-4
-6
εNd i
0.703
0.705
0.707
0.709
(87Sr /86Sr)i

Figure 5

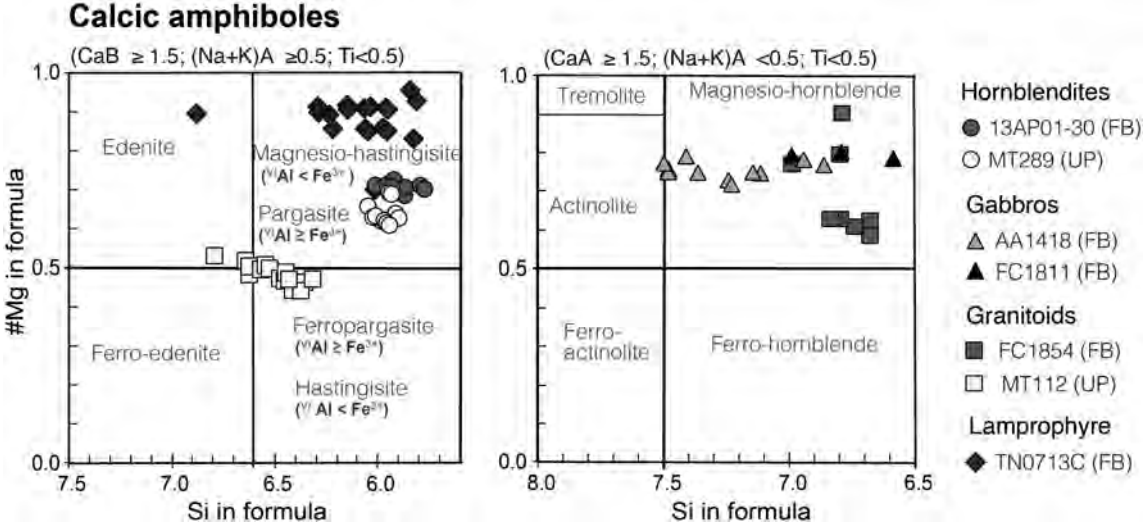
Calcic amphiboles
(CaB ≥ 1.5; (Na+K)A ≥0.5; Ti<0.5)
(CaA ≥ 1.5; (Na+K)A <0.5; Ti<0.5)
#Mg in formula
Si in formula
Edenite
Magnesio-hastingisite
(VIAl < Fe3+)
Pargasite
(VIAl ≥ Fe3+)
Ferro-edenite
Ferropargasite
(VIAl ≥ Fe3+)
Hastingisite
(VIAl < Fe3+)
Tremolite
Magnesio-hornblende
Actinolite
Ferro-actinolite
Ferro-hornblende
Hornblendites
13AP01-30 (FB)
MT289 (UP)
Gabbros
AA1418 (FB)
FC1811 (FB)
Granitoids
FC1854 (FB)
MT112 (UP)
Lamprophyre
TN0713C (FB)

Figure 6

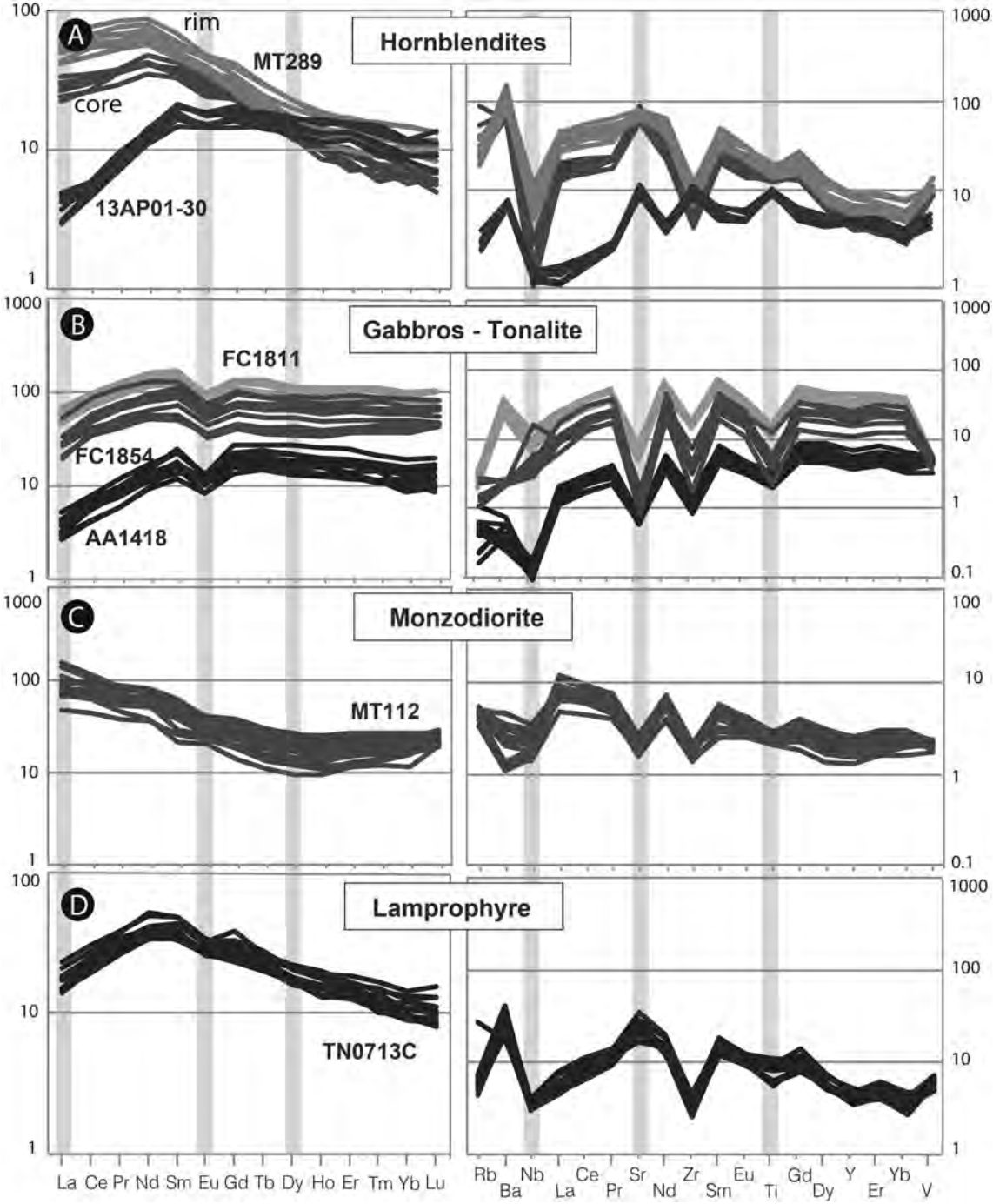
A
rim
MT289
core
13AP01-30
Hornblendites
B
FC1811
FC1854
AA1418
Gabbros - Tonalite
C
MT112
Monzodiorite
D
TN0713C
Lamprophyre
La Ce Pr Nd Sm Eu Gd Tb Dy Ho Er Tm Yb Lu
Rb Ba Nb La Ce Pr Sr Nd Zr Sm Eu Ti Gd Dy Y Er Yb V

Figure 7

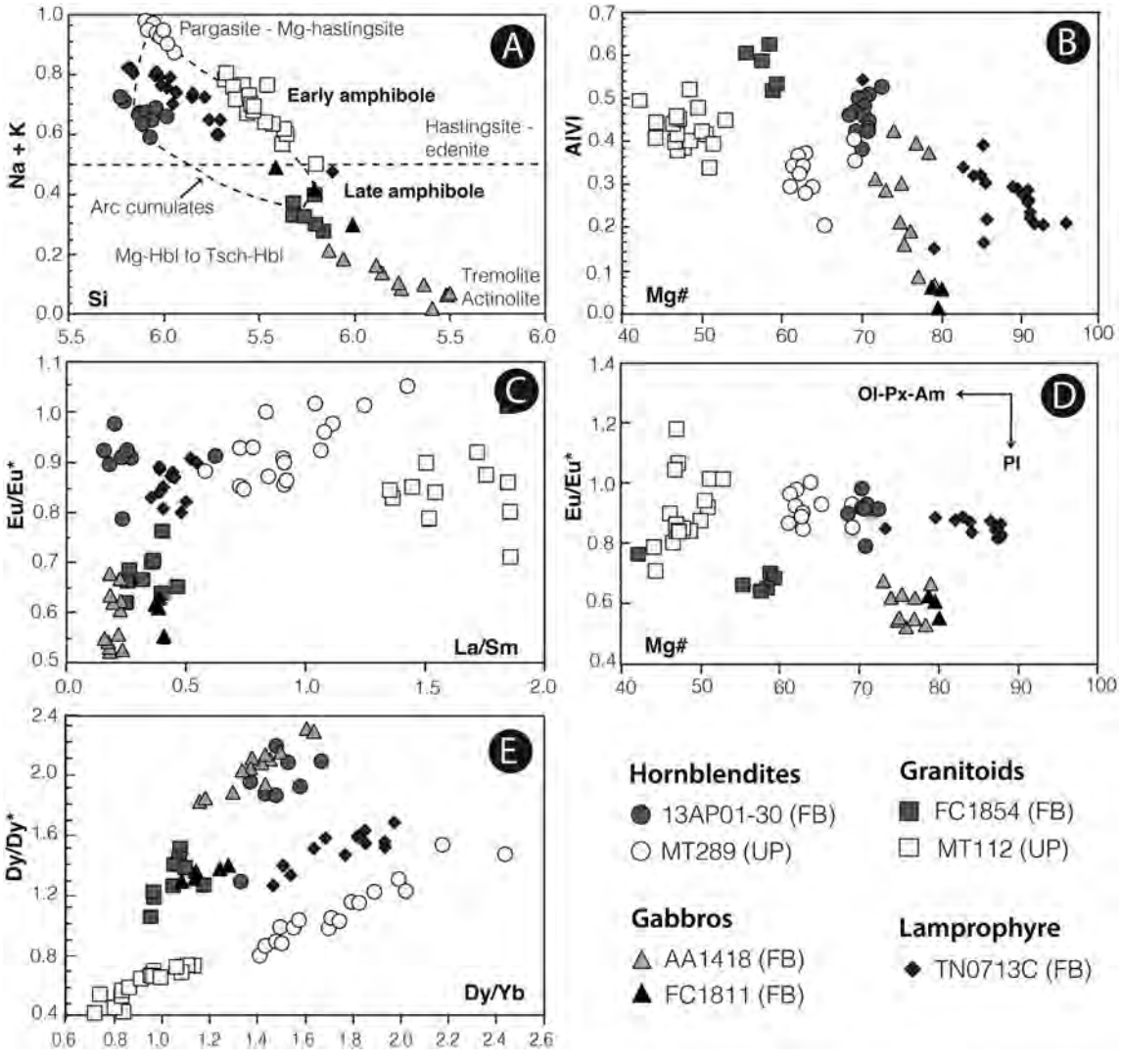
A
Pargasite - Mg-hastingsite
Early amphibole
Hastingsite - edenite
Late amphibole
Arc cumulates
Mg-Hbl to Tsch-Hbl
Tremolite Actinolite
Na + K
Si
B
AlVI
Mg#
C
Eu/Eu*
La/Sm
D
Ol-Px-Am
Pl
Eu/Eu*
Mg#
E
Dy/Dy*
Dy/Yb
Hornblendites
13AP01-30 (FB)
MT289 (UP)
Granitoids
FC1854 (FB)
MT112 (UP)
Gabbros
AA1418 (FB)
FC1811 (FB)
Lamprophyre
TN0713C (FB)

Figure 8

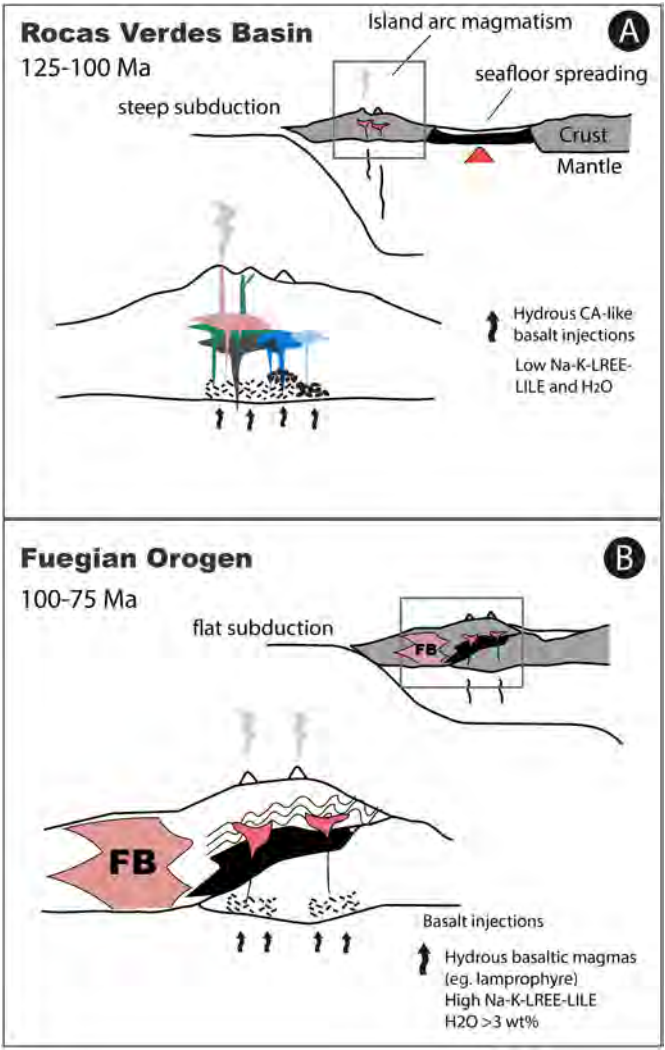
Rocas Verdes Basin
125-100 Ma
Island arc magmatism
A
seafloor spreading
steep subduction
Crust
Mantle
Hydrous CA-like basalt injections
Low Na-K-LREE-LILE and H2O
Fuegian Orogen
100-75 Ma
B
flat subduction
FB
FB
Basalt injections
Hydrous basaltic magmas (eg. lamprophyre)
High Na-K-LREE-LILE
H2O >3 wt%

Figure 9